applied sciences

MDPI

Article

Design of an Axial Turbine for Highly Downsized Internal Combustion Engines

Lorenzo Baietta [1], Mamdouh Alshammari [1], Apostolos Pesyridis [1,2,*] and Dhrumil Gohil [2]

[1] Department of Mechanical and Aerospace Engineering, Brunel University, London UB8 3PH, UK; 1736715@brunel.ac.uk (L.B.); Mamdouh.Alshammari@brunel.ac.uk (M.A.)
[2] Metapower Limited, Northwood, Middlesex HA6 2NP, UK; 1824385@alumni.brunel.ac.uk
* Correspondence: a.pesyridis@brunel.ac.uk; Tel.: +44-(0)1895-267901

Received: 16 May 2020; Accepted: 17 August 2020; Published: 27 August 2020

Abstract: This paper describes and discusses the development of an axial turbocharger turbine concept as a potential substitute to commercial radial turbines for high-volume production. As turbo-lag is one of the main issues related to the inertia of the rotating parts in a turbocharger, leading to less responsive and drive-cycle efficient power units, the use of axial turbines, with their inherently lower inertia than radial types for the same application, enables the efficient reduction of the spool-up time of the system, to the benefit of the driving experience and emissions. However, axial turbines for this application usually show complicated blades and level of twist, leading to efficient but expensive designs compared to their radial counterparts. Based on this challenge, the idea of comparing prismatic (generally less efficient, but cheaper) and twisted 3D-bladed axial turbines showed that for lower blade aspect ratios, the efficiency is of the same order. For these reasons, many turbines with a range of different sizes were designed with both layouts (3D and prismatic blades) and compared. Further, the use of 3D optical scanning, as well as dyno-calibrated 1D engine models enabled the gathering of invaluable data to design the proposed solution and compare it to the Original Equipment Manufacturer (OEM) version. Thanks to these processes, the comparison between the proposed design and the OEM one was not limited to the performance, and also included the manufacturing costs, which were calculated via Computer Aided Manufacturing (CAM) programs, with the limitation of using only Computer Numerical Control (CNC) machining for production. To conclude, the work showed a notable performance superiority of the proposed turbine in respect to the OEM one, despite a slightly higher estimated production cost.

Keywords: axial turbine; turbocharger; turbine design; internal combustion engines; downsizing

1. Introduction

The continued research for engine efficiency improvements is one of the major challenges of recent decades, leading manufacturers to the design of highly downsized boosted engines. Among other boosting strategies, turbocharging allows the recovery of part of the exhaust gas energy, improving the overall efficiency of the power unit.

Turbochargers lead to less responsive power units because of the widely known turbo-lag effect, which is due to the inertia of the rotating parts in the system. Given the context of engine manufacturers testing different concepts to reduce this effect, for both commercial and motorsport applications, this work is about the development of a low-inertia turbocharger axial turbine, evaluating the pros and cons of several design solutions.

Turbo-lag is the primary target for improvement of present-day turbocharger manufacturers. In fact, axial turbines inherently have a lower rotational moment of inertia, but for turbocharger applications, the cost is higher than for radial ones [1]. Replacing the conventional, bulky radial turbine

with an advanced, lightweight axial device has potential to improve the transient response of the boost system and the whole vehicle, while not sacrificing steady-state performance. This defines the problem with current turbocharging technology and highlights the necessity for research on the axial turbine in the automotive environment.

Despite the above advantages, axial turbines are predominantly found in aerospace and large power generation applications. A major challenge may be found in the decrease in efficiency with a decrease in size. Hence, increases in aerodynamic efficiency are of paramount importance in the successful employment of such designs.

The aim of this work was to design a cost-effective axial turbine and to compare its performance with the Original Equipment Manufacturer (OEM) system. The decided objectives were to compare the baseline and proposed turbocharger with respect to the performance, on-engine model performance and cost, to conduct aerodynamic and structural design and analysis and to determine the new turbocharger concept design.

The idea is to initially evaluate the performance (mainly efficiency) difference between prismatic and twisted-blade turbines for a range of different sizes. In fact, as one of the issues of axial turbines compared to radial ones is the production cost, the use of low-aspect-ratio blades, in such a way as to minimize the difference between the use of 3D-optimized turbines and prismatic turbines, should allow for more cost-effective solutions to be implemented.

In fact, if the aspect ratio is smaller, the relative velocity "seen" by the blade tip section is closer to that seen at the hub in the case of more elongated blades, where the two sections are farther apart by design, reducing the advantage of the use of twisted blades with specifically oriented airfoils. After selecting a specific engine to develop the axial turbine, in this case a Ford EcoBoost 1.0 L, several Computer Aided Engineering (CAE) techniques will be used to verify the idea and to obtain the best possible solution. The OEM turbocharger will be 3D-scanned with a blue light technology stereoscopic optical system to acquire accurate geometrical data and calculate several engineering properties. A Ricardo Wave 1D engine model, calibrated on the dyno, will be run to obtain the boundary conditions for the design of the new turbine. Several turbines will be preliminarily designed and optimized with AxSTREAM and their performances evaluated considering many parameters, mainly focusing on the reduction of the turbocharger spool-up time.

The generated turbine preliminary Computer Aided Designing (CAD) and the scanned OEM turbine mesh will be used along with Computer Aided Manufacturing (CAM) programs to estimate the production cost (with manufacturing cost prediction outsourced to an external company) of the different solutions.

After selecting a final axial turbine design from the predesigned ones, it will be validated with the generation of complete maps within the AxSTREAM streamline solver and further optimized with CFD simulations of increasing precision in AxCFD. 2D cascade simulations will be used to optimize the stator and rotor airfoils. Then, axisymmetric CFD simulations will run at several operating points to quickly investigate the suitability of the generated design for the whole power unit operating range. To conclude, full 3D CFD and FEA simulations will be conducted to obtain more accurate values and complete the design process of the turbine.

The results of the simulations will demonstrate the superiority of the proposed turbine, both from the turbo-lag mitigation and efficiency point of view, with a similar estimated production cost, confirming the level of attainment of project objectives.

Finally, a novel key performance indicator (KPI), the spool-up factor ($\frac{d\omega}{dP}$), was introduced and its importance demonstrated.

2. Background of Turbochargers

2.1. Turbochargers

Turbochargers are systems that exploit exhaust gas energy to precompress the air charge before it enters the internal combustion (IC) engine cycle, allowing for better engine efficiency and higher specific power.

A turbine, mechanically connected to a compressor by a shaft, is blown by the exhaust gases and transmits its rotation to the compressor. Subsequently, a charge air cooler is used to increase the air density and further improve the volumetric efficiency of the engine.

2.2. Machine Types

Conventional turbochargers implement radial rotors for both turbine and compressor rotors. This is mainly due to their relatively low cost, the wider range of volumetric flow they can operate under and the higher-pressure ratio per stage they can withstand. Other turbochargers feature axial and mixed flow impellers. The former is of particular interest because of its inherently lower inertia and higher efficiency for certain operative ranges, despite often being more expensive than conventional radial machines.

In recent decades, many solutions have been proposed by OEMs and researchers in the field to achieve design improvements from the manufacturing or pure performance point of view. Among these, most recently in [2], it was shown that additive manufacturing techniques, inparticular Selective Laser Melting (SLM), offer advantages over conventional manufacturing techniques, such as design freedom, flexible processing and onsite manufacturing. This can reduce inertia on the turbines, allowing for very complex and efficient aerodynamics and mechanical designs (e.g., a honeycomb-like inner structure allowing for lower rotating mass, thus maintaining acceptable structural requirements). On the other hand, others, such as Volvo, use a separate electrically driven compressor connected to an air tank to blow the turbine with compressed air from the high-pressure tank when the driver is accelerating to reduce the spool-up time [3]. The most significative recent development in this field is, however, the DualBoost design proposed by Honeywell. Honeywell produced an innovative ultralow inertia system, called DualBoost, featuring an axial turbine and a double-sided compressor.

The axial turbine presents excellent flow capacity and better efficiency compared to a conventional radial turbine under flow conditions typical of gasoline engines. Further, this layout allowed for a perfect match between the axial turbine's high speed (being necessary for higher efficiency) and that of the reduced-diameter double-sided (back-to-back type) compressor impeller, proving to be an effective choice for LMP1 cars, such as the 24 Hours of Le Mans winner, the Porsche 919 Hybrid.

The DualBoost design is of interest to motorsport because of its fitness with the new 2021 F1 power unit regulations, which in removing the Motor Generator Unit-heat (MGU-H), will need ultraperforming low-inertia turbochargers. Further, the application of this kind of layout in an electric machine would be a novelty (to the best of the authors' knowledge) and would find application in the next-generation power units for the Fédération Internationale de l'Automobile World Endurance Championship (FIA WEC) [4].

Variable-Geometry Turbines (VGTs) are a category of machines allowing for a better match between turbine geometry and off-design flow conditions. They are among the other main research subjects, as well discussed by [5]. This review discussed the benefit of the implementation of different VGT techniques despite the increased cost of the systems. They showed that the most common and efficient VGT nozzle types to be implemented resulted in pivoting stators and sliding vanes, also pointing out a trend in implementing hydraulically and in particular, electrically actuated systems for a more precise geometry control than the standard pneumatic actuated types. VGTs have recently been used in other automotive-related applications, such as waste heat recovery [6].

2.3. Aerodynamics

The aerodynamics of turbomachinery are strictly dependent on the type of machine selected for an application: radial, axial or mixed flow. In this regard, axial machine (which are the focus of this work) cascade aerodynamics will be the main focus in the design of the blades. Cascades are the series of airfoils obtained by cutting the turbomachine with a conical/cylindrical surface coaxial with the machine rotation axis. Flattening the cascade surface, it is common practice to analyze the flow with virtual velocity triangles obtained by the composition of the actual flow velocity (in the inertial frame) "hitting" the rotor and the rotational velocity of the rotor itself in order to design the airfoil for the relative flow velocity and angle.

Two main types of turbines can be used for this type of application: impulse or reaction turbines. The former does not have any pressure change in the rotor, which spins because of the change in direction of a high-velocity flow due to the curvature of the blade; the latter type distributes the pressure drop both in the stator and rotor, while the rotor does not change the direction of the flow as much as impulse turbines, but is nozzle-shaped. Moreover, reaction turbines are mainly used for machines that must develop torque from a high-pressure fluid. For this reason, the reaction turbine type is the preferred choice for the considered application.

The aerodynamic design of modern turbomachines could be split into three major parts: preliminary design, 1D–2D meanline and streamline analysis and optimization, profiling, blade design and final 3D analysis. This process will be further described in the methodology section; however, as the preliminary design and 1D–2D analyses are based on thermo-fluid-dynamic and simplified mechanical calculations, it is important to model the performance with empirically based loss models accounting for phenomena such as profile losses, tip losses, stalling and so forth.

2.4. Losses

Different types of losses can be identified for turbines: the most important being profile losses, secondary losses, tip clearance losses and trailing-edge losses. Profile losses are due to the wall friction on the blade and to the airfoil boundary layers, wakes and potentially shock waves. Secondary losses are mainly generated in the annulus passages by transverse pressure gradients and inertial forces. Secondary losses give origin to vortical flow structures because of the annulus boundary layer entering the blade row and can account to up to 50% of the total aerodynamics losses [7]. Tip clearance losses are those generated by the passage of fluid between the blade tip and the casing because of the pressure difference between the suction and pressure sides of the rotor blade. These losses are reduced in the case of shrouded blades as the shroud acts as an endplate, also making the rotor more robust, but increasing the inertia and the manufacturing costs.

To conclude this brief summary, trailing-edge losses are those caused by the suction and pressure side boundary layers meeting at the trailing edge of the blades, which are usually slightly smoothed (as opposed to being perfectly sharp edges) because of structural requirements, and therefore generating a stationary separated shear layer and eventually shock waves.

2.5. Loss Models

A fair number of loss model have been proposed by several authors; the most significant ones for the present work are briefly introduced here.

Ainley and Mathieson [8] developed a model from empirical data mainly based on flow parameters with calculations performed at a reference diameter for each stage. The pressure loss is not influenced by the Mach number, and the gas outlet angle is not influenced by the incidence angle.

Further improvements were achieved by Dunham and Came, who revisited the Ainley and Mathieson model, adding a correction for profile losses for Mach > 1, introducing an empirical parametric formulation for secondary losses based on blade aerodynamic load and geometry and formulating a nonlinear tip loss estimate, overall improving the performance prediction accuracy [7].

Kacker and Okapuu enhanced the accuracy of the same model by adding a trailing edge loss coefficient, improving the Reynolds number and Mach number correlation for secondary losses and including shock losses.

Another widely used model is that developed by Craig and Cox. This model, which is built on several experimental acquisitions, uses several input parameters including the Reynolds number, Mach number, blade aspect ratio, blade angles and passage geometry, also taking into account the surface roughness.

The Kacker–Okapuu and Craig–Cox models are among the most used models, and [9] showed they are in quite good agreement in a variety of situations. However, as a result of their study, Ennila, A.S.B. [10] suggested that for small-scale axial turbines, the Kacker–Okapuu model gives the closest values to the CFD simulations. For these reasons, the model employed here was more significantly based on the Kacker–Okapuu model.

Generally, as illustrated by [1] and other authors, axial turbine turbochargers tend to increase the manufacturing cost. However, as shown by [11] for organic Rankine cycle turbines, axial turbines show a higher cost to produced power ratio, therefore potentially making them more suitable for applications where extra power exploited by the turbine can be recovered and converted into electrical energy.

3. Methodology

The methodology used for this work is summarized in the following schematic diagram (Figure 1).

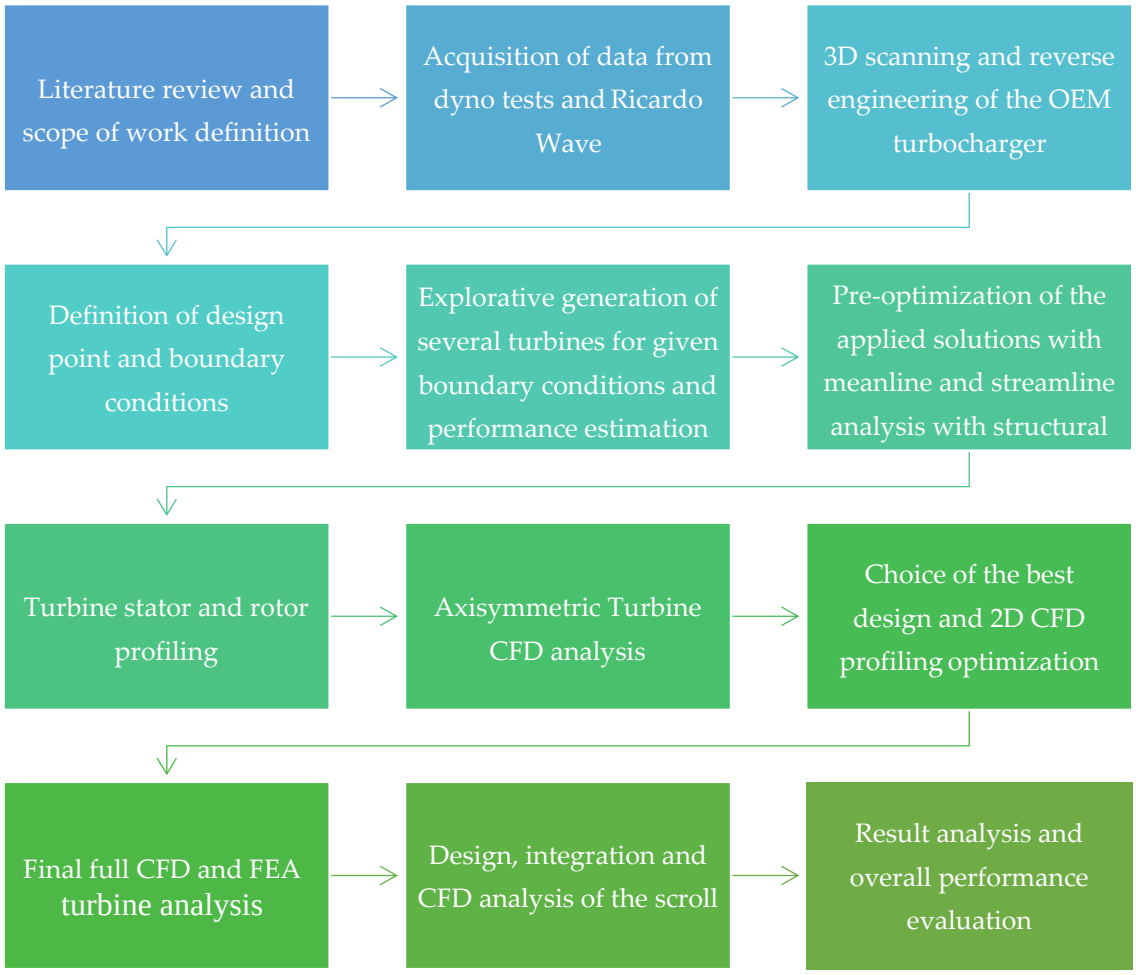

Figure 1. Methodology flow chart. CFD: Computational Fluid Dynamics; Finite Element Analysis (FEA); OEM: Original Equipment Manufacturer.

3.1. Definition of the Project

The chosen engine is a Ford EcoBoost 1.0 L. The reasons for this choice are mainly related to the state of the art represented by this engine and the availability of this engine at Brunel University London's Centre for Advanced Powertrains and Fuels, as well as the availability of experimental results for this engine relevant to this work, meaning the availability of accurate data for this particular model. Further, an original spare turbocharger was available to be analyzed and studied without the need to remove the engine turbocharger.

3.2. Data Acquisition, 3D Scanning and Reverse Engineering of the OEM Turbocharger

The initial data to acquire were mainly thermo-fluid-dynamic engine parameters. These were obtained from a Ricardo Wave engine model developed and calibrated by Ford, shown in Figure 2, and from engine dyno testing performed by the University powertrain research group (Figure 3).

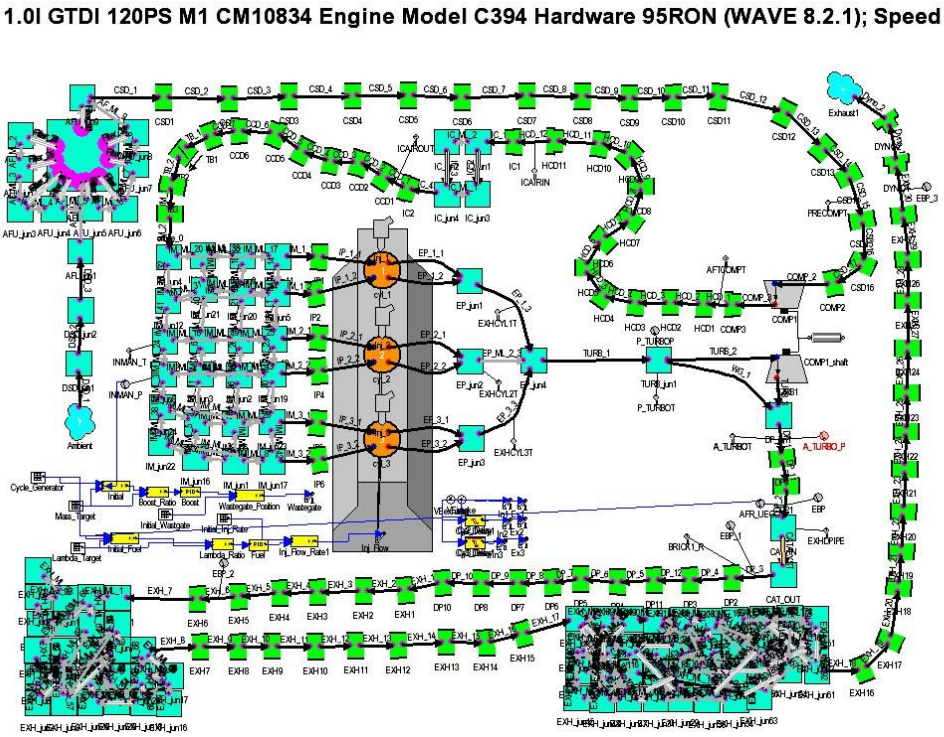

Figure 2. Ricardo Wave Ford engine model.

The data from the Ricardo Wave model were already calibrated thanks to Ford, and Brunel University performed dyno testing (Figure 3). After the acquisition of the thermo-fluid-dynamic data, it was necessary to acquire the geometric information about the original turbocharger. This process was conducted for two main reasons: Firstly, these data were used to define the geometric/spatial constrains for the new unit and to evaluate the mass properties of the rotors. Secondly, these parts were planned to be 3D-scanned in order to use the resulting mesh for CFD validation comparing the results from the numerical analysis to the experimental data given by Ford.

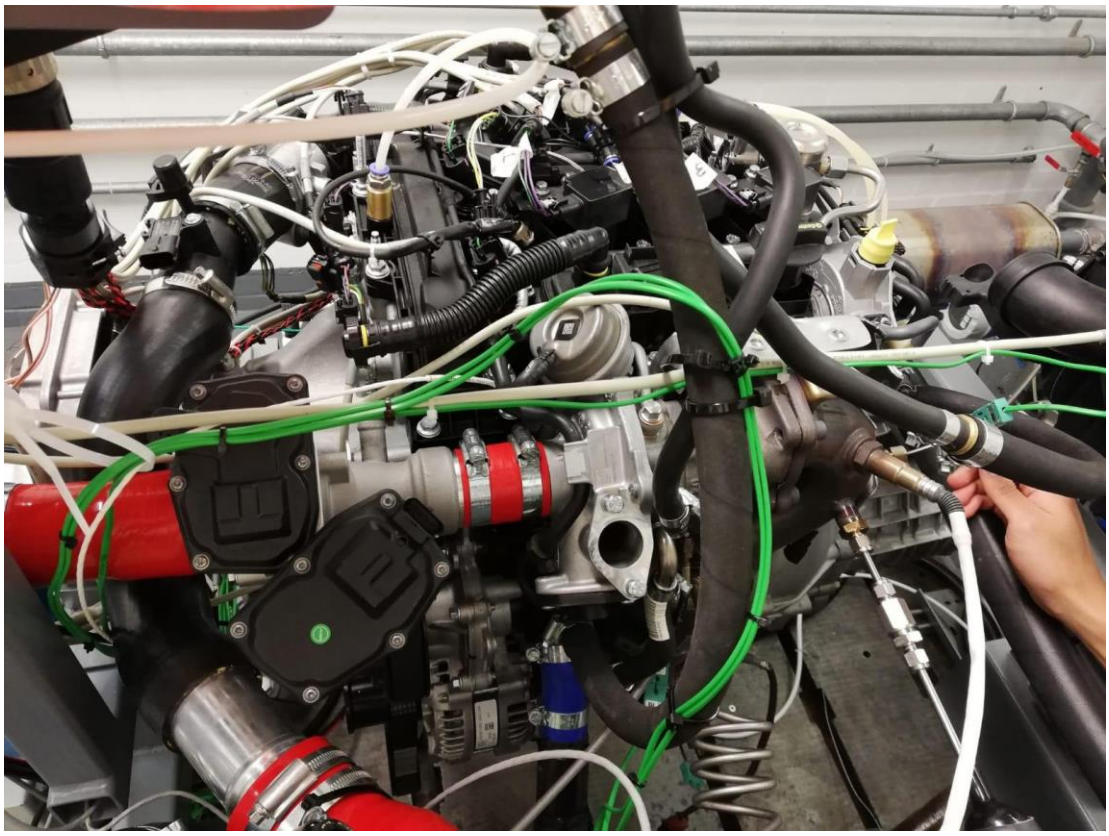

Figure 3. Engine on the dyno before testing.

3.3. Definition of Design Point and Boundary Conditions

The data from the Ricardo Wave-simulated 1D engine model at full load were used to define the initial boundary conditions for the design of the turbine. The reason for choosing full load is that the axial turbine's main purpose is to reduce the inertia compared to a radial one to improve the response, and thus it is supposed to be more important in an aggressive driving style. The design point was moved at 2000 engine rpm because of the higher necessity of torque at lower regimes when accelerating from stationary. However, as explained in the Results section, the final design point was then definitively set to 4000 rpm, as the 2000 rpm one did not allow for a suitable turbine at maximum engine revolutions (revs).

In order to ensure a proper match between the original compressor and the turbine, it was important to make sure that for a given engine operating point, the turbine was able to give enough power for the compressor at given shaft rpm values. Initially, this condition was checked for the design point. Then, as discussed in Section 3.5, a map was created to check the suitability of the turbine for the whole operative range.

The main geometric constraint parameters to control in order to obtain a low-inertia axial turbine are those related to the mass of the turbine and its distribution or its moment of inertia relative to the rotation axis. Approximating the turbine rotor to a cylindrical element (as shown in Figure 4), there is a clear strong dependence of the moment inertia with the radius of the turbine and linear dependence with the length.

$$I = \frac{1}{2}\pi\rho l\left(r_t^4 - r_h^4\right) \tag{1}$$

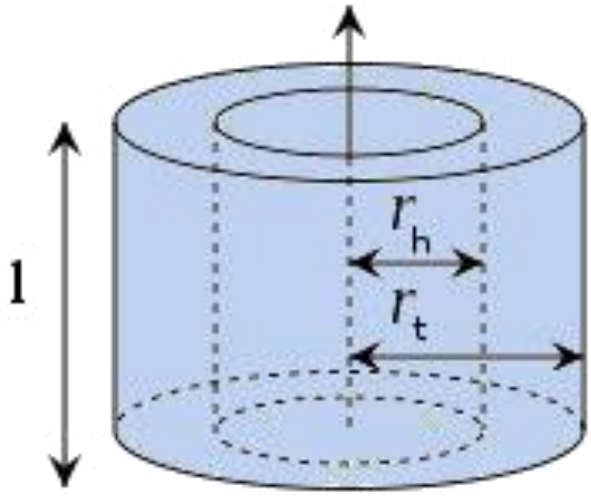

Figure 4. Simplified rotor blade model.

For this reason, the main geometric parameters to control in the design of the turbine will be the hub radius (r_h) and the blade height (r_t–r_h) (being important for the aerodynamic design of the blade). A simple Excel file was created to obtain further data as an input for the preliminary design of the turbine (Figure 5) through simple calculations.

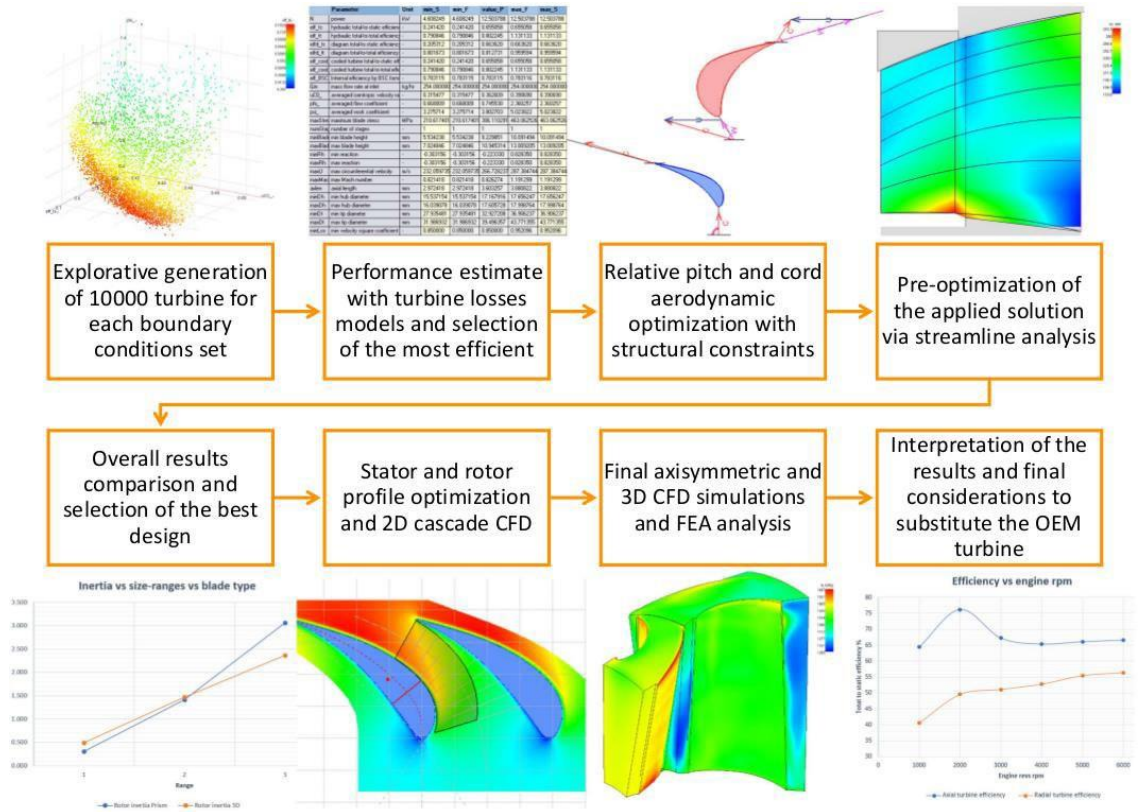

Figure 5. Schematic of the turbine design methodology.

The data obtained from measuring/scanning the original turbocharger were used as a reference and as limitations to the size of the new turbine assembly, as it must interface with the existing system (exhaust manifold, turbocharger bearing and cooling housing, exhaust pipe, etc.).

3.4. Turbine Design Methodology Summary

The turbine design methodology is briefly summarized in the following figure and explained in detail in the following paragraphs. Performant turbines can be designed thanks to increasingly accurate Design of Experiments (DoE) methods. Over 10,000 turbines were generated for each type (6 types), then selected ones were optimized to reduce the losses.

3.5. Explorative Generation of Several Turbines for Given Boundary Conditions and Performance Estimation

AxSTREAM allows for the generation and evaluation of the performance of several possible design solutions to a given physical problem within the defined constraints and boundary conditions. For this work, it was decided to use a reaction turbine type, as it is the more suitable type for high pressure ratios, as discussed in the literature review.

AxSTREAM was then used to map the generated preliminary designs and select any of them based on their performance (Figure 6). Therefore, the AxSTREAM preliminary design module was used to perform an initial explorative generation of turbines for the design point.

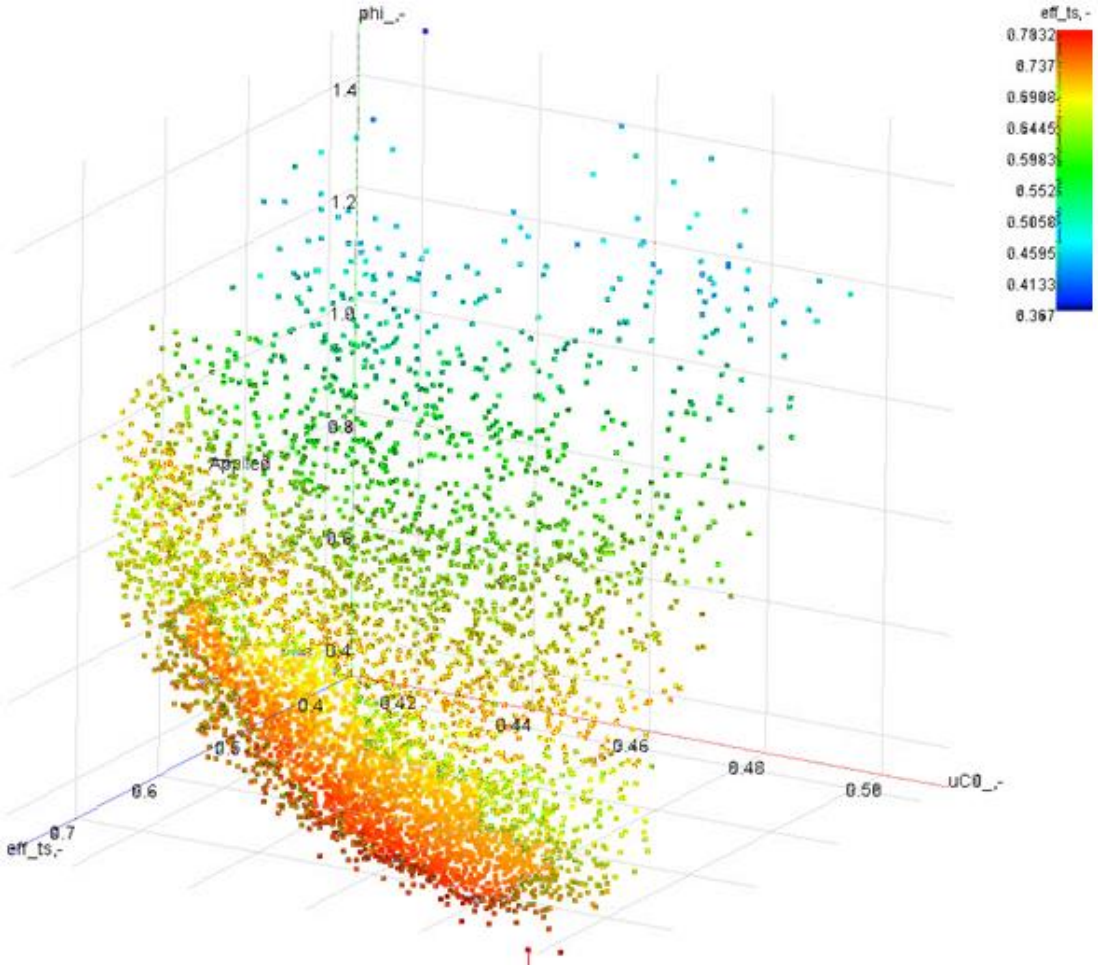

Figure 6. Plot of all the generated preliminary turbine design performance parameters (total to static efficiency (eff_ts), blade speed ratio (U/C0) and flow coefficient (phi)).

AxSTREAM evaluates and validates all the possible design solutions within the range of the boundary conditions and constraints set by the user (Table 1). Initially, over 1,000,000 preliminary designs were evaluated across very wide ranges in order to pick the best possible design starting point from the total to static efficiency point of view. Although this way of operating may seem to

give excellent results at first sight, it does not allow one to properly evaluate less thermodynamically efficient solutions, which may be relevant because of lower inertia, cost or other reasons.

Table 1. Table of predesigned boundary conditions (AxSTREAM Inverse Task solver).

Data	Unit	Min	Max
Boundary Conditions			
Inlet Total Pressure	kPa	262	262
Inlet Total Enthalpy	kJ/kg	1597	1597
Stat. Pressure at Outlet	kPa	124	124
Mass Flow Rate	kg/h	254	254
Inlet Flow Rate	tan. deg	90	90
Shaft Rotational Speed	rpm	178,422	178,422
Parameters			
Hub Diameter	mm	9	18
Rotor Diameter Ratio (D2/D1)	-	1	1
1st Stage Blade Height l1	mm	5	10
Hub Reaction	-	0	0.800
Isentropic Velocities Ratio (u/Co)	-	0.2400	0.4600
Heat Drop Gradient (H_z/H_1)	-	0.800	1.000
Meridional Velocities Gradient (Cm_z/Cm_1)	-	0.800	1.200
Module Admission Ratio	-	1	1
Constraints			
Number of Stages	-	1	1
Hub Diameter Limit	mm	1.000	10,000.000
Tip Diameter Limit	mm	1.000	50.000

Therefore, the design space was divided into multiple parts with different ranges of hub diameter and blade height. Each of these ranges was further divided in two types: the 3D blade type and the prismatic blade type, allowing performance evaluation of both. In fact, the impact of the production cost of the turbine must be considered as well as its pure performance. 3D-optimized blades are certainly more effective than the cheapest and easier-to-manufacture extruded blades for medium-high aspect ratio blades. For this reason, it was thought that blades with lower aspect ratios would have seen more similar flow velocity triangles spanwise than longer blades, and in the case of comparable performance (efficiency, power, inertia etc.), were going to cost less than optimized twisted blades. The cars fitting this engine are indeed city cars produced in large numbers, with increasing production rate, which doubled to 9.8 m units (excluding spare parts) in 2018, according to [12]; therefore, it is clear that even small savings on the production cost may have a very big impact on company revenue.

3.6. Preoptimization of the Applied Solutions with Meanline and Streamline Analysis

The preliminary solution, consisting of the principal meridional channel dimensions, thermodynamic parameters and initial velocity triangles and blade chord data (Figure 7), is then exported to the preoptimization module of AxSTREAM, allowing for aerodynamic optimization of the blades' relative pitch and chord of the selected design solution, also considering the structural requirements with an automatic parametrized stress calculator (not the Finite Element (FE) method). This module recalculates the thermo-fluid-dynamic parameters via meanline analysis and allows the designer to manually edit the meridional channel section after checking the physical properties' contour in order to further improve the efficiency of the machine.

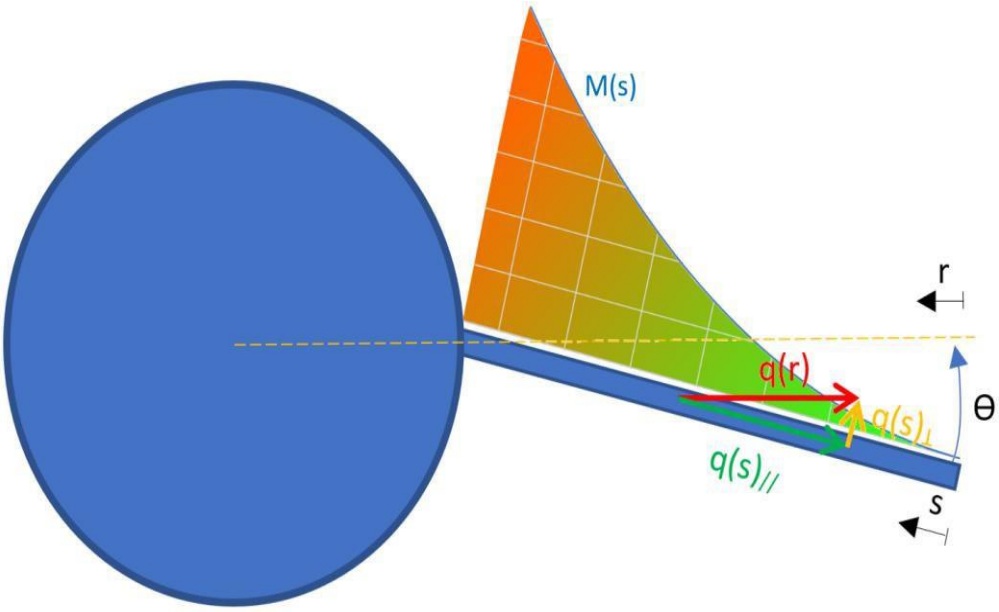

Figure 7. Simplified load and bending moment plot schematic of a prismatic leaned blade under centrifugal loads. (M(s): bending moment; q: load; r; turbine radius; s; blade span).

Then, an axisymmetric 2D thermodynamics solver was used to calculate the streamlines distribution in the meridional channel, as well as increasing the precision of the meanline calculator. In the case of 3D blades, this module was also used to perform a minimization of the incidence angle and change the blade twist parameters in such a way as to allow for better off-design performance, reducing the chance of stalling at different flow conditions.

A map of the turbine was then calculated with the same solver to check the suitability for the application in off-design points. However, a weakness of this solver is that it does not consider the actual profile shape, as it is based on 1D–2D calculations and loss models. For this reason, the final turbine suitability was to be determined via increasingly accurate CFD simulations.

3.7. Turbine Stator and Rotor Profiling

The design of the airfoils was performed in the AxSTREAM profiling module. AxSTREAM automatically proposes the optimized profile for the middle section, and starting from that and from the already calculated parameters and flow condition, it proposes an initial airfoil solution for all the other sections. However, many changes to airfoil parameters are performed, mainly on the stagger angle, inlet wedge angle and outlet wedge angle (as they do not affect the optimized camber line shape), in order to have acceptable Mach numbers over the airfoil and respect the Buri criterion (Figure 8). Further, a second optimization process based on the reduction of profile losses with a DoE method was performed with the airfoil optimization tool embedded in the AxSTREAM profiling module, allowing for a semiautomated airfoil shape improvement.

The profiling module is also used to control the turbine manufacturability by checking critical areas, such as the size of the throat of the nozzles, or more generally, the overall turbine solidity, in such a way to ensure it can be machined.

After the airfoil optimization and manufacturability check, 2D cascade CFD (RANS) analysis was performed at various spanwise sections to control the effectiveness of the generated airfoils before passing the data to the CFD module, which typically requires much longer setup and solving times.

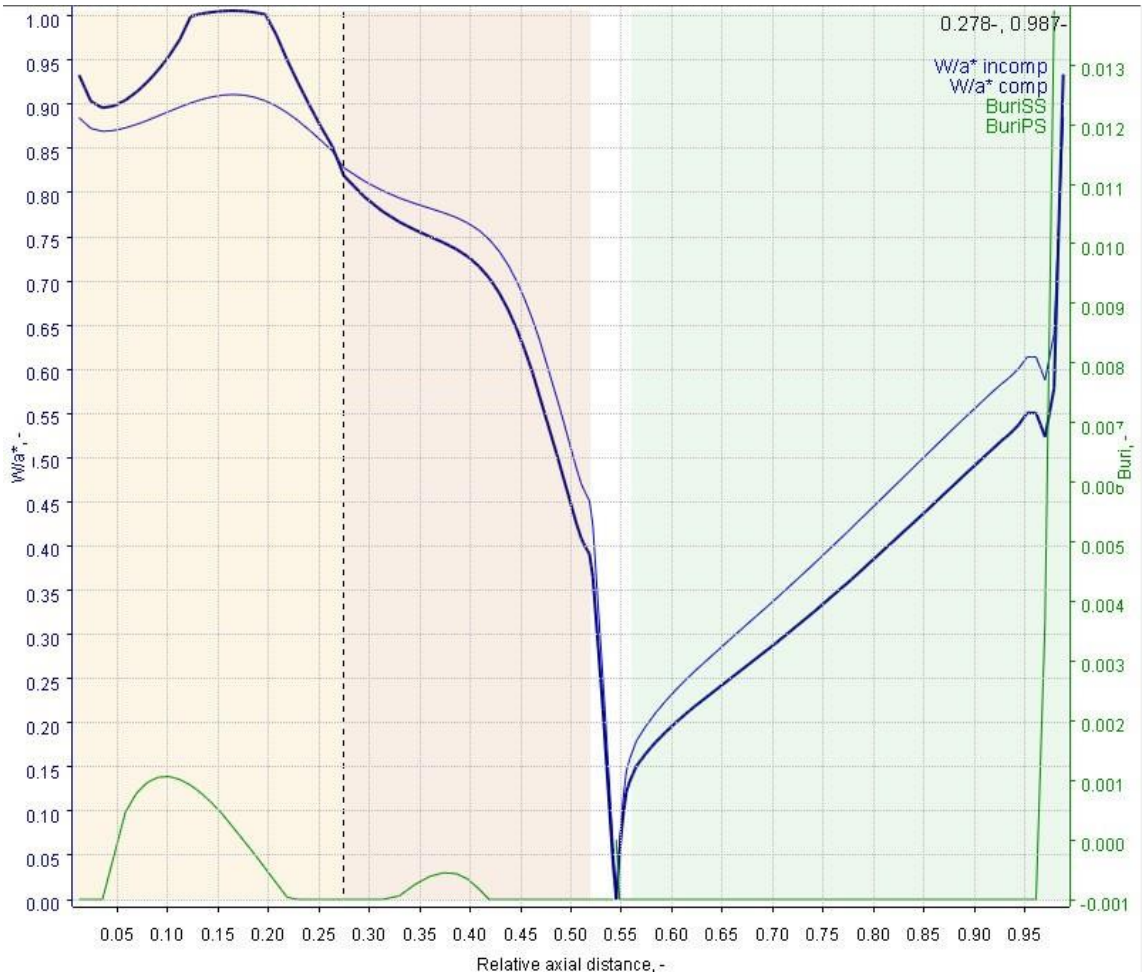

Figure 8. Streamwise Mach numbers (blue) and Buri criterion values (green) over a stator profile section. ("comp": compressible; "incomp": incompressible; "SS": surface side; "PS": pressure side).

This module was also used to control the leaning, sweeping and bowing of stators and rotor blades to obtain further efficiency improvements (Figure 9). This operation was performed infrequently, as the bending stress on the blades increases substantially due to the centrifugal loads, as shown in the following simplified calculations for the simple case of a prismatic leaned blade.

As the principle of superposition is valid for this kind of problem, only the centrifugal loads are considered for this demonstration, as the contribution of the aerodynamics and mechanical load does not affect the partial solution and can be added separately. Therefore, defining the specific centrifugal load in cylindrical coordinates as:

$$q(r) = \rho\omega^2\left(r_t - \frac{r}{2}\right) \tag{2}$$

then considering the bladewise coordinate,

$$s = r\ \cos(\theta) \tag{3}$$

the centrifugal load can be decomposed in a bladewise load $q(s)_{//}$ and a shear load $q(s)_{\perp}$, as in Figure 8.

In particular, the presence of the transverse load with centrifugal force, which evidently would not happen with a radially extruded blade, is the factor generating the added bending moment. In fact, considering

$$q(s) = \rho\omega^2\left(r_t - \frac{s}{2\cos(\theta)}\right)\sin(\theta) \tag{4}$$

the shear force is:

$$T = \int_0^{s^*} q(s)\, ds \tag{5}$$

and the bending moment is:

$$M(s) = \int_0^{s^*} T(s)\, ds = \rho\omega^2 \sin(\theta)\left(r_t \frac{s^2}{2} - \frac{s^3}{12\cos(\theta)}\right) \tag{6}$$

with the plot shown in Figure 8 displaying a strong bending load at the blade root.

Moreover, despite the fact that bowed, swept or leaned blades often display better performance, they also come with a significantly more challenging manufacturing process, as they inherently have undercut areas requiring additional CNC milling time, precision and capability.

The stuck-up airfoil section was also controlled to evaluate the influence of different choices, both from the aerothermal and structural point of view. Centroid axis, leading edge and trailing edge stuck-up types were tested in different combinations both for the stator and rotor, but the preferred one remained the standard centroid stuck-up type.

To conclude, when profiling the blade, the blade surface curvature was controlled with the colored contours shown in Figure 9 to obtain a smooth blade while avoiding aerodynamically and structurally problematic areas (potential stalling, stagnation and breaking).

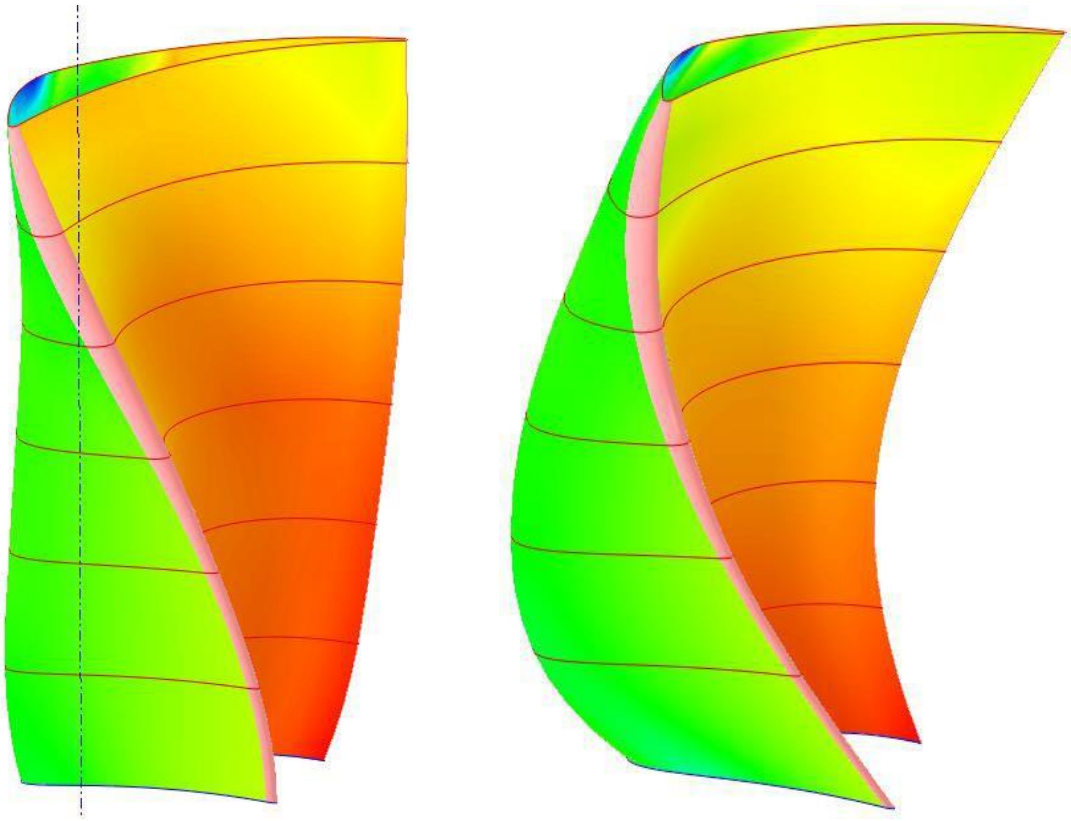

Figure 9. Comparison between a standard radial blade (**left**) and a high-performance bow-type one (**right**).

3.8. Turbine CFD Analysis

Axisymmetric CFD (RANS) analyses were conducted to rapidly validate the previous design and obtain more accurate results regarding the performance of the machine with AxCFD (Figure 10) with respect to the streamline calculator. These calculations were performed on a mesh shaped on the

deviation angles calculated with the 2D streamline analysis and camber surface of the stator and rotor blades. This method is particularly useful to control the distribution of the main parameters along the flow path.

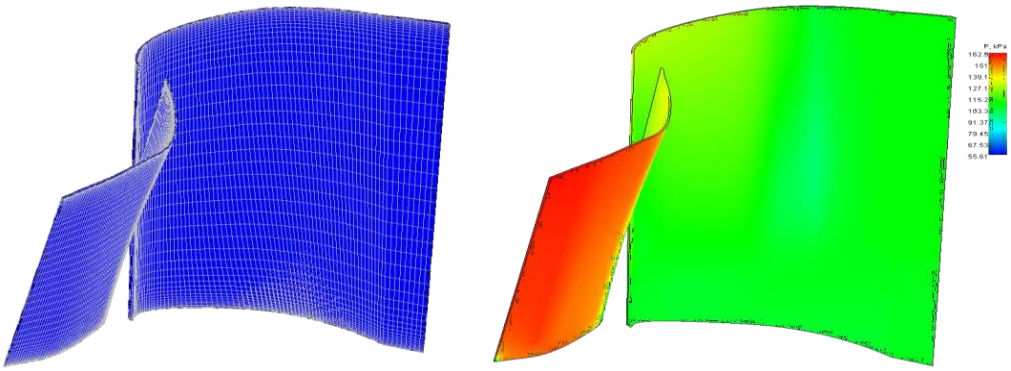

Figure 10. Axisymmetric CFD simulation mesh and results (pressure scene) view.

The simplicity of these simulations allows for the prevalidation of a blade design with relatively quick calculations; the design will eventually be adjusted in the profiling module, before conducting full 3D CFD simulations.

After the final modifications, the turbine was then simulated by means of 3D periodic CFD simulations. Mesh sensitivity studies were performed in order to determine the most convenient mesh size for the work and are reported in Figure 11. The target mesh size was chosen to be around 400,000 elements, as it showed an excellent balance between precision and solving time.

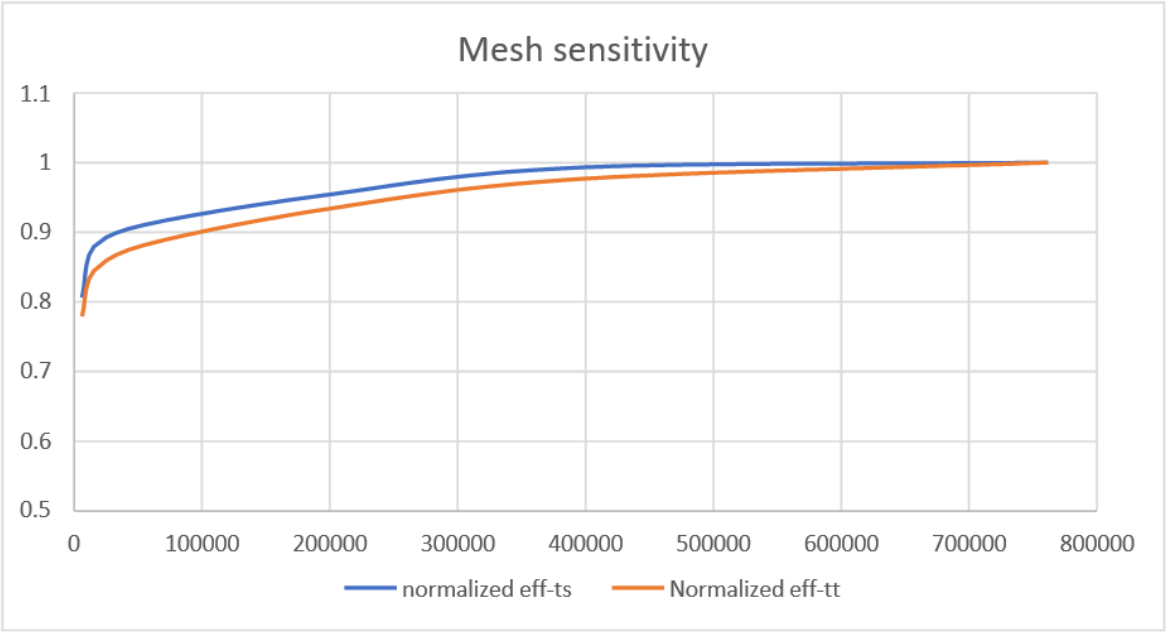

Figure 11. Efficiency results from CFD mesh sensitivity analysis.

Both for axisymmetric and 3D CFD, the validation was performed at six engine speeds from 1000 rpm to 6000 rpm, with every 1000 rpm increase being at full load, in order to make sure of the suitability of the turbine for the whole engine operating range.

3.9. Choice of Best Design and 2D CFD Profiling Optimization

The final design was chosen based on three criteria: low inertia, low cost and acceptable efficiency. The lower-inertia designs, as will be discussed in the Results section, are not usually the most efficient, and the most efficient designs are not the most cost-effective. Therefore, the choice of the final solution weights the pros and cons of several KPIs to find the optimal one for the chosen application.

3.10. Final FEA Turbine Analysis

The final solution was analyzed through FEA with AxFEA and ANSYS to validate the design and eventually make minor changes to the airfoils. The reason for using different software was due to the different control of certain simulation parameters which cannot be achieved in AxFEA.

In AxFEA, the loads acting on the blade were transferred to the FE solver from the CFD module solution to check the structural compliance of the turbine, thus finalizing the design of the rotor and the stator. The loads were taken from the CFD solution performed at max rpm (not at the design point), as this represented the most critical operating condition for the turbine.

It is, however, important to note that the simulations are conservative and should be performed with a more complete and computationally expensive model, because the blade temperature was considered to be uniform, while in fact the OEM turbocharger has a liquid cooling system which actually effectively removes heat from the turbine shaft, and therefore from the turbine rotor itself, making it colder and thus stronger (Figure 12).

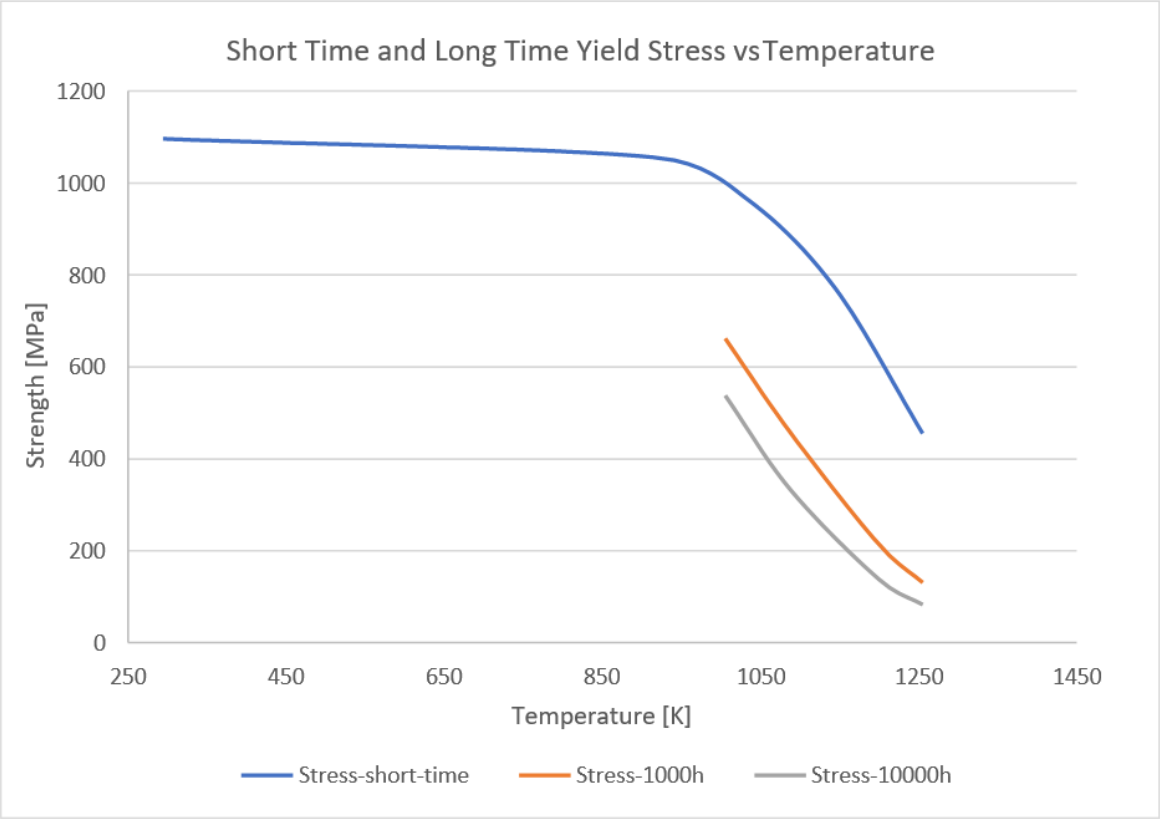

Figure 12. Inconel-738 performance plots calculated with data by Inco.

3.11. Choice of the Rotor Material

As the rotor is spinning at very high speeds (up to 200,000 rpm), it was decided to use different materials for the stator and rotor. For the stator, a common Inconel-718 was more than sufficient, while the stronger Inconel-738 was chosen for the rotor, the performance of which is illustrated in Figure 12.

3.12. CFD Simulation Details

CFD simulations were performed with H and O grid meshes and the k-ω Shear Stress Transport (SST) model. The O mesh was used to model the boundary layer around the blade, as this is ideal for capturing the typical flow behavior in the area with an elevated number of prism layers of increasing size. The H grid is a classic mesh type for turbomachinery, with a lower computational cost compared to polyhedral meshes, allowing for timesaving but effective modelling of the fluid dynamics problem. The reason for using the k-ω SST turbulence models stays in the effective use of the k-ω and k-ε turbulence models in different parts of the fluid domain. In fact, while the k-ω model is used in the boundary layer, thanks to the SST formulation, the k-ε model is used for the flow outside the boundary layer, overall making the simulation less sensitive to the initial turbulence level (a feature of particular importance for this case, as it depends on the engine operating point, exhaust and scroll design, etc.).

The simulations were started with a low-order RANS solver and coarser grid. Upon convergence, the grid was improved to a finer one, determined with the mesh sensitivity study, until convergence. At this point, the CFD solver was upgraded to a higher order in such a way to have a more precise solution. The operation of solving the problem with increasing mesh quality and solver order allows the reduction of the CPU time (which can often be more than 12 h for just the stator and rotor periodic simulation with an Intel i7-7700HQ at 3.8 GHz).

Finally, the mesh quality was always controlled, ensuring that the mesh Jacobian determinant ratio, which is an index of the mesh distortion, was always greater than zero and with the majority of the elements (more than 95% in the most precise simulations) having higher quality values (Figure 13).

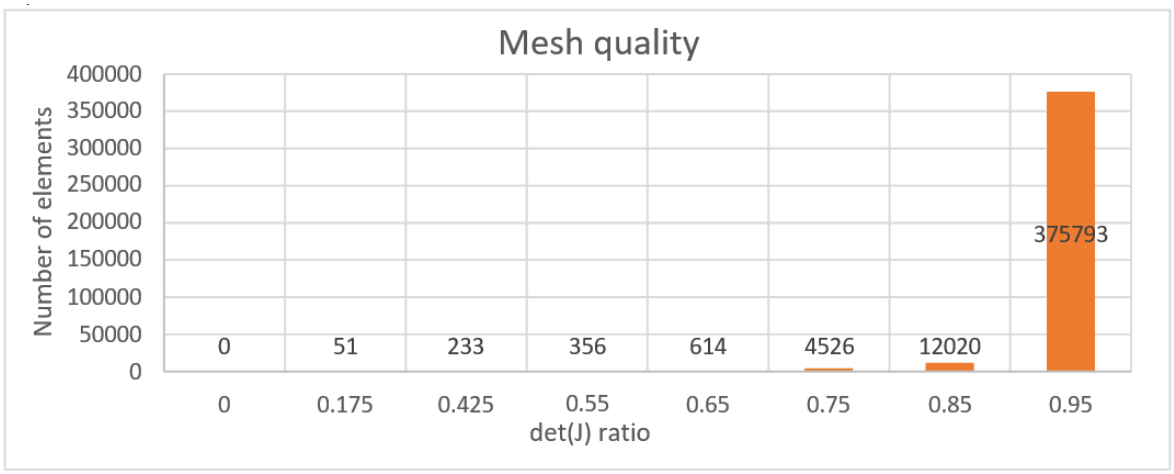

Figure 13. Typical CFD mesh quality distribution graph—number of elements versus Jacobian determinant det(J) ratio

Figure 14 illustrates an example of the correction of a low-quality mesh with volumes with a low Jacobian ratio to a higher quality one in order to ensure a correct cell growth rate and appropriate size in every part of the fluid domain. These corrections were mainly performed acting on the O-grid thickness and number of elements (basically the boundary layer mesh zone) and mesh refinements at the leading edge and trailing edges (especially on the suction side of the blades, in order to properly catch any possible separation bubble or stall).

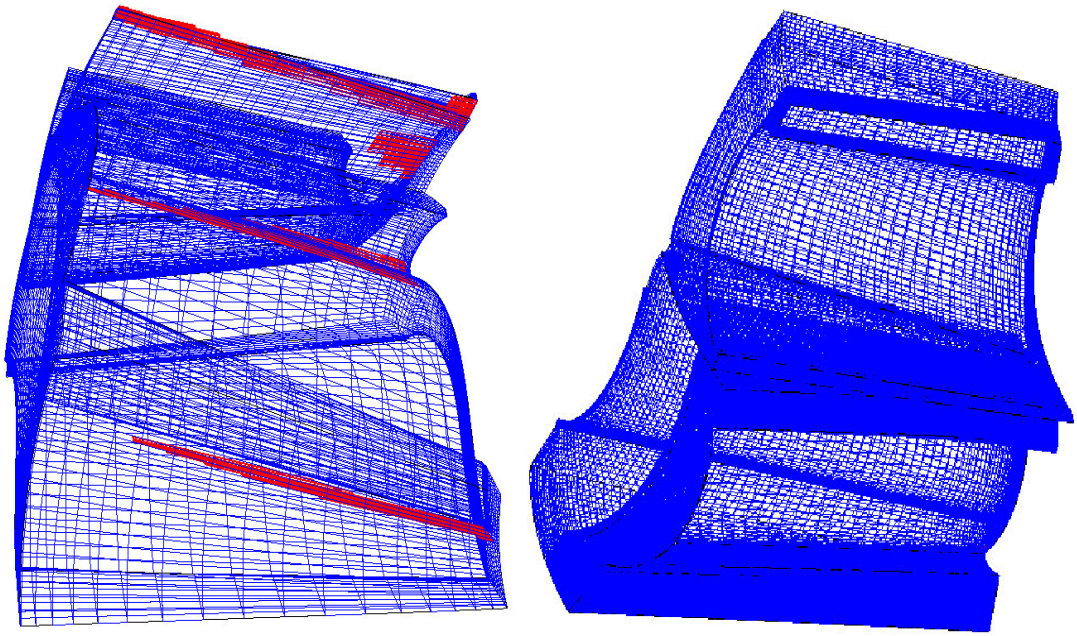

Figure 14. Left: Highly distorted basic mesh with many elements with det(J) ratio ≤ 0 (red elements). Right: Corrected high-quality mesh with the same geometry, ensuring stable and accurate CFD calculations.

4. Results

4.1. Turbine Design Preliminary Results

As illustrated in Figure 15, the low difference in efficiency for small-aspect ratio blades for prismatic and 3D blades is validated, as it is in the order of 3%. After verifying this hypothesis with the design of turbines for low engine revs (Table 2), these turbines were mapped in order to investigate the suitability of the designs for the requirement of the compressor and engine at higher pressure ratios and mass flow rates. In Table 2 velocity ratio (u/c0) are provided (tip speed, u, and absolute flow velocity, C0); width and height d_h and H_blade respectively. This process demonstrated that designing the turbine at lower engine revs may result in the turbine going into a sonic choking regime too early at higher engine revs, and therefore not producing enough power for the compressor. The representative condition was achieved at 154,609 revolutions per minute (rpm) with a flow velocity (absolute) of 571 m/s and an efficiency of 49.52%.

Table 2. Summary of Design of Experiment details for lower engine revolutions.

DoE	Range 1		Range 2		Range 3		Range 4	
	Min	**Max**	**Min**	**Max**	**Min**	**Max**	**Min**	**Max**
u/c0	0.269	0.638	0.284	0.666	0.354	0.737	0.425	0.808
d_h	9	15	12	17	17	22	22	27
H_blade	5	15	4	15	4	15	4	15
rpm	154,609	@ 2000 rpm (engine), turbine pressure ratio 1.67						
Co	571							
eff_ts OEM	49.52							

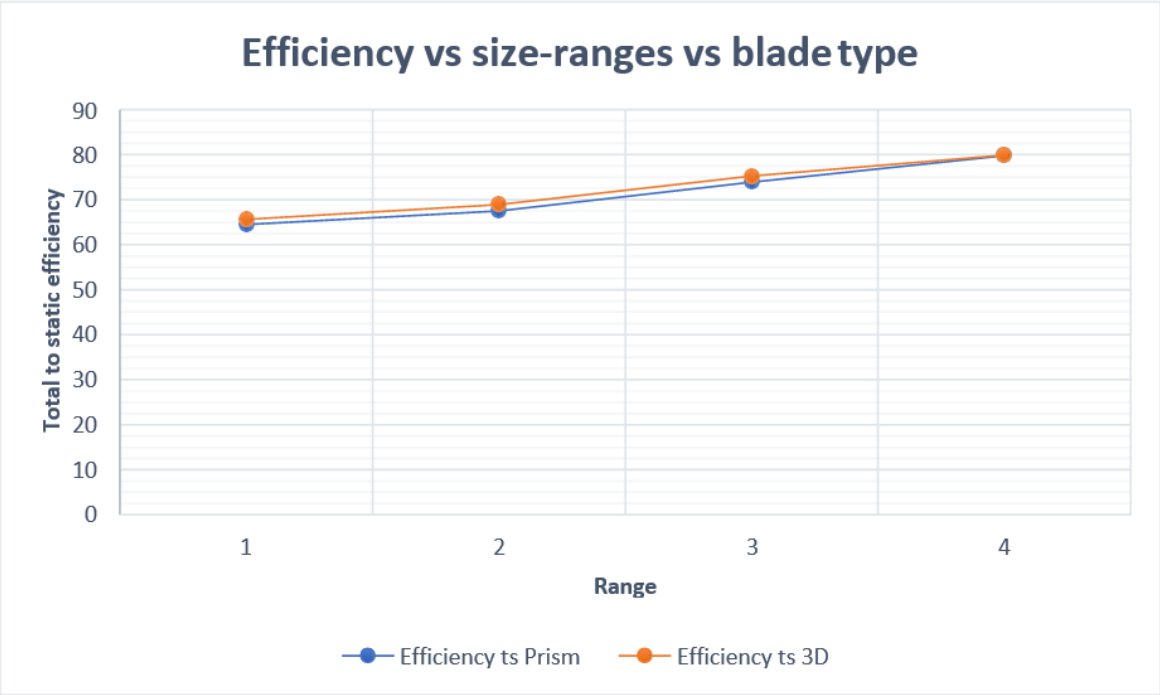

Figure 15. Efficiency vs. size ranges and blade types for low engine revolution turbines.

The design point was then shifted to 4000 engine rpm, as this is the point where the OEM compressor has its higher efficiency. In fact, as illustrated in the Ricardo Wave results table (Table 3), the turbine has its max efficiency at the highest turbocharger shaft rpm. Moreover, the turbine is always slightly bypassed by the Electronic Control Unit (ECU), as demonstrated by the large difference in mass flow rate between the compressor and turbine (Table 3). This happens because the OEM turbine was fitted to the engine without being specifically designed for it, while the compressor works without any bypass at full performance. Further, this operating point was closer to the design point chosen by [13] for a similar Ford EcoBoost engine (design point at 5000 engine rpm for a 1600 cc engine), thus further confirming the suitability of such a decision. Table 4 shows the distinct size ranges for the design of the turbines at the new design point. It was decided to divide the design space into four size ranges with diameters that are multiples of the OEM turbine minimum hub diameter, while the blade height ranges were selected to allow for Hypothesis 1 to be verified, as specified above.

Table 4 highlights the aggregated input data for a turbine design range at the design point, and was used to calculate part of the input data in the AxSTREAM preliminary design module from others available from the Ricardo Wave turbocharger solution data.

Table 3. Overall turbocharger rotor performance.

Turbocharger data	Range 1		Range 2		Range 3		Baseline
Properties	**Prismatic**	**3D**	**Prismatic**	**3D**	**Prismatic**	**3D**	**Radial**
Shaft inertia kg*m^2	7.78E-07	8.46E-07	8.17E-07	9.08E-07	8.09E-07	8.24E-07	1.38E-07
Compressor inertia kg*m^2	3.48E-06	3.48E-06	3.48E-06	3.48E-06	3.48E-06	3.48E-06	3.48E-06
Total turbine plus shaft inertia kg*m^2	2.38E-06	3.40E-06	8.13E-06	8.46E-06	1.66E-05	1.30E-05	5.30E-06
Total turbocharger rotors inertia kg*m^2	5.85E-06	6.88E-06	1.16E-05	1.19E-05	2.01E-05	1.65E-05	8.77E-06
Total dω/dP (kW*s)^-1	1.13E-04	9.13E-05	6.39E-05	6.21E-05	3.77E-05	4.64E-05	5.74E-05
Normalized Total dω/dP (kW*s)^-1	1.96	1.59	1.11	1.08	0.66	0.81	1

Table 4. Summary of Design of Experiment details at the final design point.

DoE	Range 1		Range 2		Range 3		Range 4	
	Min	**Max**	**Min**	**Max**	**Min**	**Max**	**Min**	**Max**
u/c0	0.248853	0.497706	0.366731	0.615584	0.484608	0.733461	0.602486	0.720364
d_h	9	18	18	27	27	36	36	45
H_blade	5	10	5	10	5	10	5	5
rpm	178,422	@ 4000 rpm (engine), turbine pressure ratio 2.01					* Not performed due to nonsuitable $d\omega/dP$ value	
Co	713.2762							
eff_ts OEM	52.7133							

Specifically, the mass flow ratio (MFR) from the compressor was used, as the OEM turbine is always slightly bypassed. The other main data were the inlet turbine temperature, outlet pressure and shaft rpm. Further, a constraint on the results was the turbine power, which must be equal to or higher than that required by the compressor.

The results of the design of the turbines at the final design point are illustrated in the following tables and Figures 16 and 17 for Range 1 (min. velocity ratio range) for prismatic and 3D blades, respectively; Figures 18 and 19 for Range 2 (min. velocity ratio range) for prismatic and 3D blades, respectively; and Figures 20 and 21 for Range 3 (min. velocity ratio range) for prismatic and 3D blades, respectively. The red lines (and labels) are the iso-efficiency curves, while the blue lines (and labels) are the constant power curves.

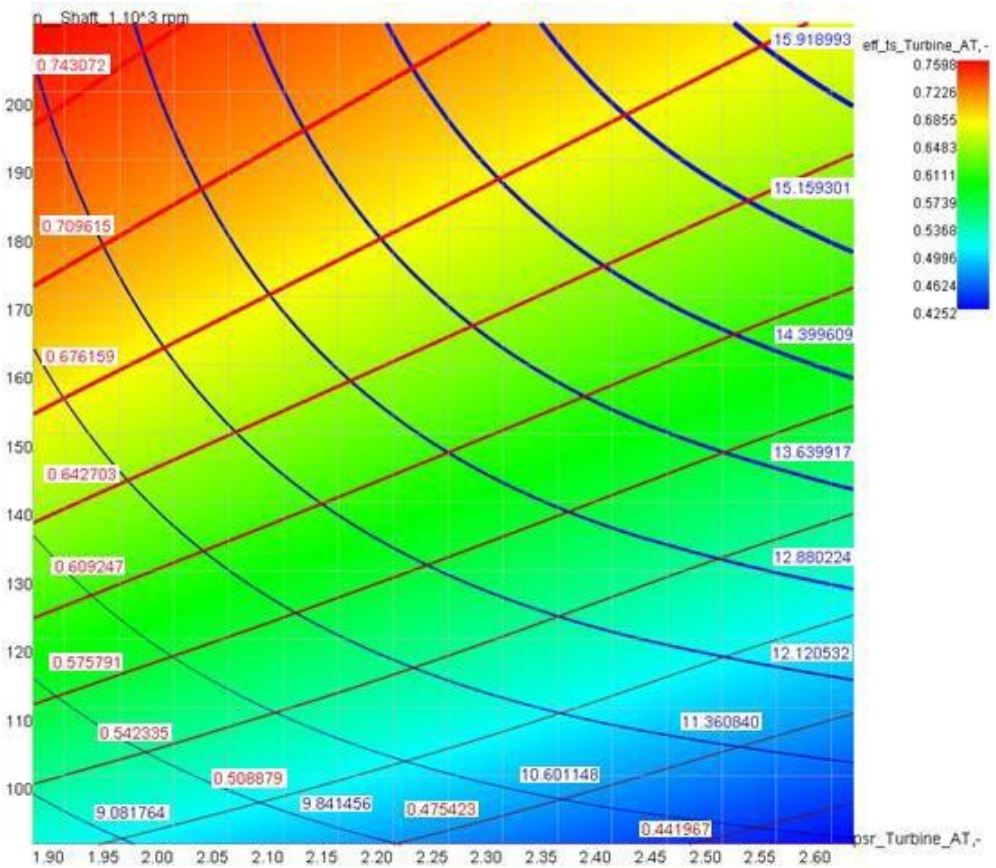

Figure 16. Prismatic Range 1 turbine map (*y*-axis: shaft speed in rpm (1000 s); *x*-axis: turbine pressure ratio). The legend at the top right-hand side indicates the range of total-to-static turbine efficiency.

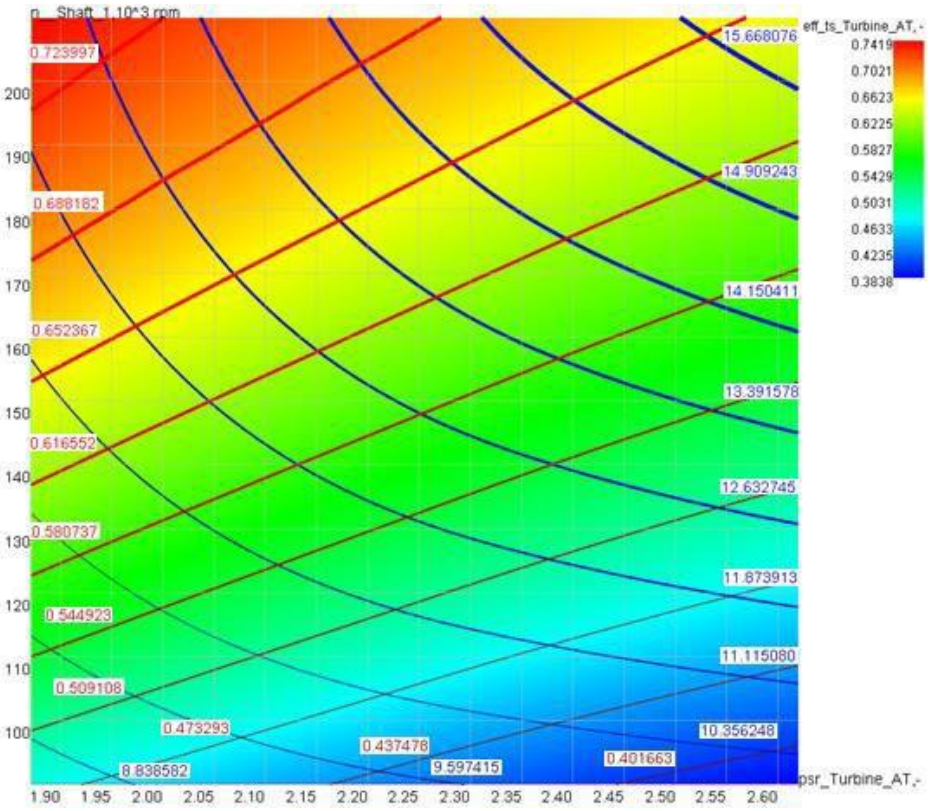

Figure 17. 3D Range 1 turbine map (*y*-axis: shaft speed in rpm (1000 s); *x*-axis: turbine pressure ratio). The legend at the top right-hand side indicates the range of total-to-static turbine efficiency.

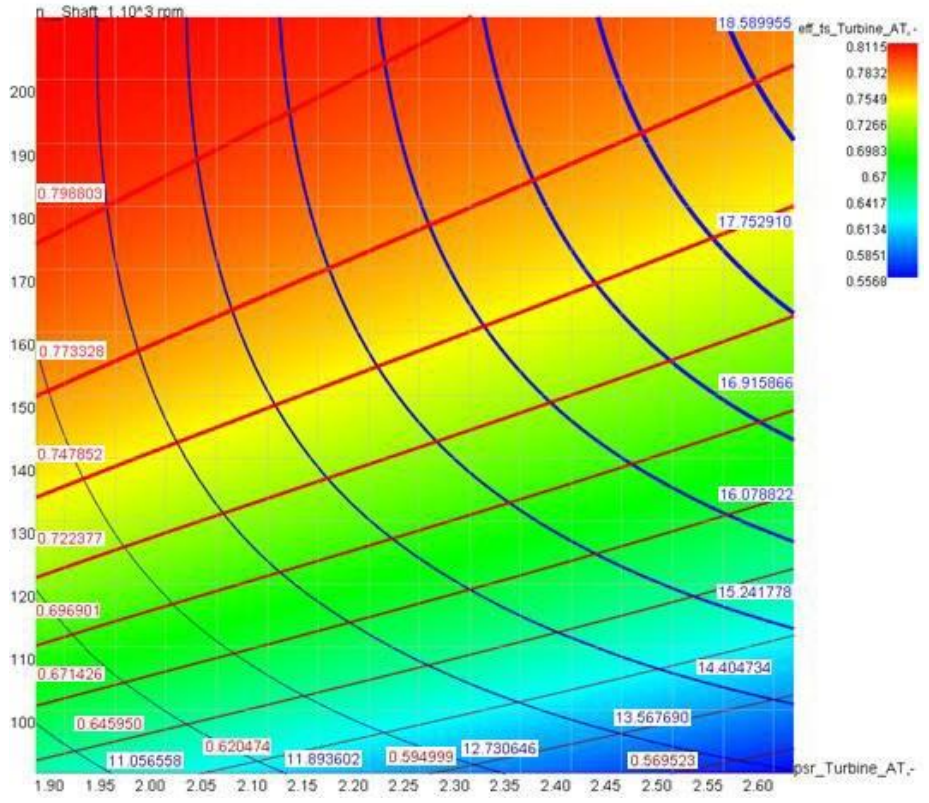

Figure 18. Prismatic Range 2 turbine map (*y*-axis: shaft speed in rpm (1000 s); *x*-axis: turbine pressure ratio). The legend at the top right-hand side indicates the range of total-to-static turbine efficiency.

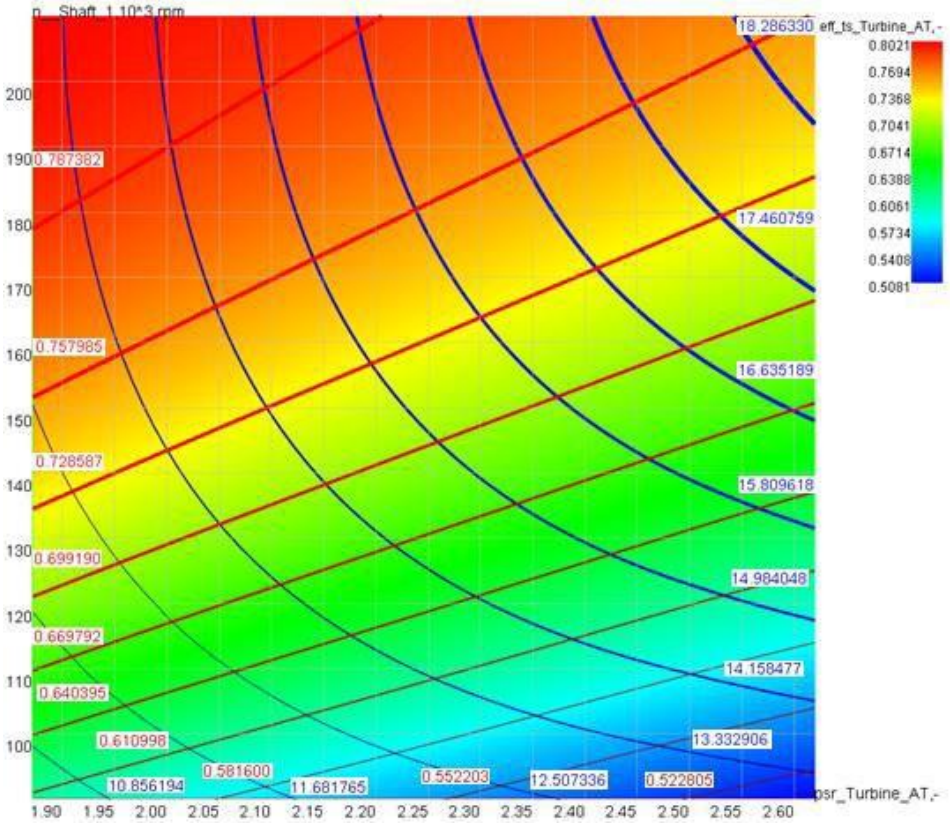

Figure 19. 3D Range 2 turbine map (*y*-axis: shaft speed in rpm (1000 s); *x*-axis: turbine pressure ratio). The legend at the top right-hand side indicates the range of total-to-static turbine efficiency.

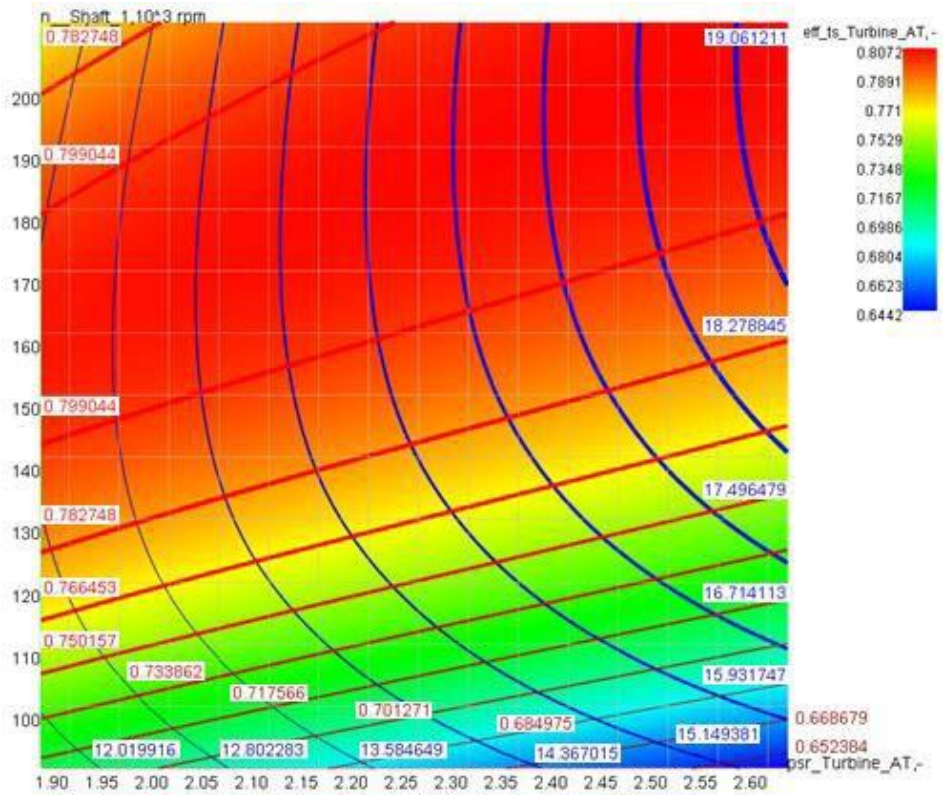

Figure 20. Prismatic Range 3 turbine map (*y*-axis: shaft speed in rpm (1000 s); *x*-axis: turbine pressure ratio). The legend at the top right-hand side indicates the range of total-to-static turbine efficiency.

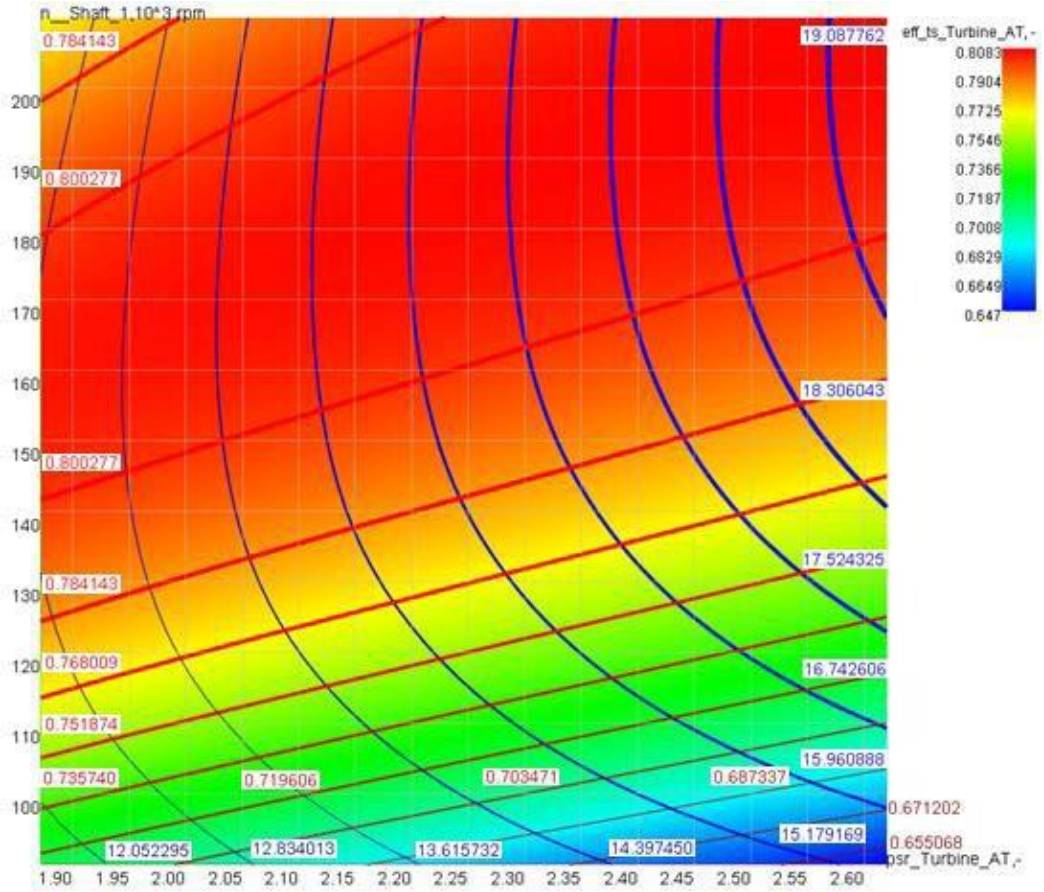

Figure 21. 3D Range 3 turbine map (*y*-axis: shaft speed in rpm (1000 s); *x*-axis: turbine pressure ratio). The legend at the top right-hand side indicates the range of total-to-static turbine efficiency.

Since the reason for designing an axial turbine was mainly related to the possibility of reducing the inertia of the rotor to reduce the spool-up time of the turbocharger, the normalized inertia was the first value to analyze. It soon became apparent that looking at the rotational moment of inertia only would have excluded the solutions in Range 2 and Range 3.

However, a few notes are needed regarding this matter. Firstly, the mechanical design was not yet optimized, as the focus of the preliminary design was on the thermo-fluid-dynamics point of view, thus excluding any machining to remove weight. Additionally, regarding the prismatic blades, it is important to remember that they use the same airfoil shape and size in all the spanwise sections, while 3D blades not only change the shape, often with the thinner airfoil being closer to the tip, but are also tapered, therefore having less mass on the tip and reducing the inertia compared to prismatic blades for the same size range. This is particularly evident in larger turbines, where there are higher numbers of blades in order to cover a bigger hub circumference; also being inherently bigger in chord than the smaller ones, thus affecting the rotor inertia even more, as shown in Figure 22. In fact, in the graph, 3D turbines display lower inertia for higher size ranges.

Although the inertia values seemed to exclude the turbines in the second size range from the viable solutions, it was also evident that higher size ranges corresponded to higher efficiencies, at least for the small turbine dimensions that were studied in this work (Figure 23). This is not only shown by the results of the design conducted within this study, but also by other authors, such as in [13], that showed the correlation when comparing the efficiencies for different blade speed ratios (U/c_0), where U depends only on the diameter of the turbine for a given turbocharger shaft rpm value and c_0 only depends on the inlet total enthalpy.

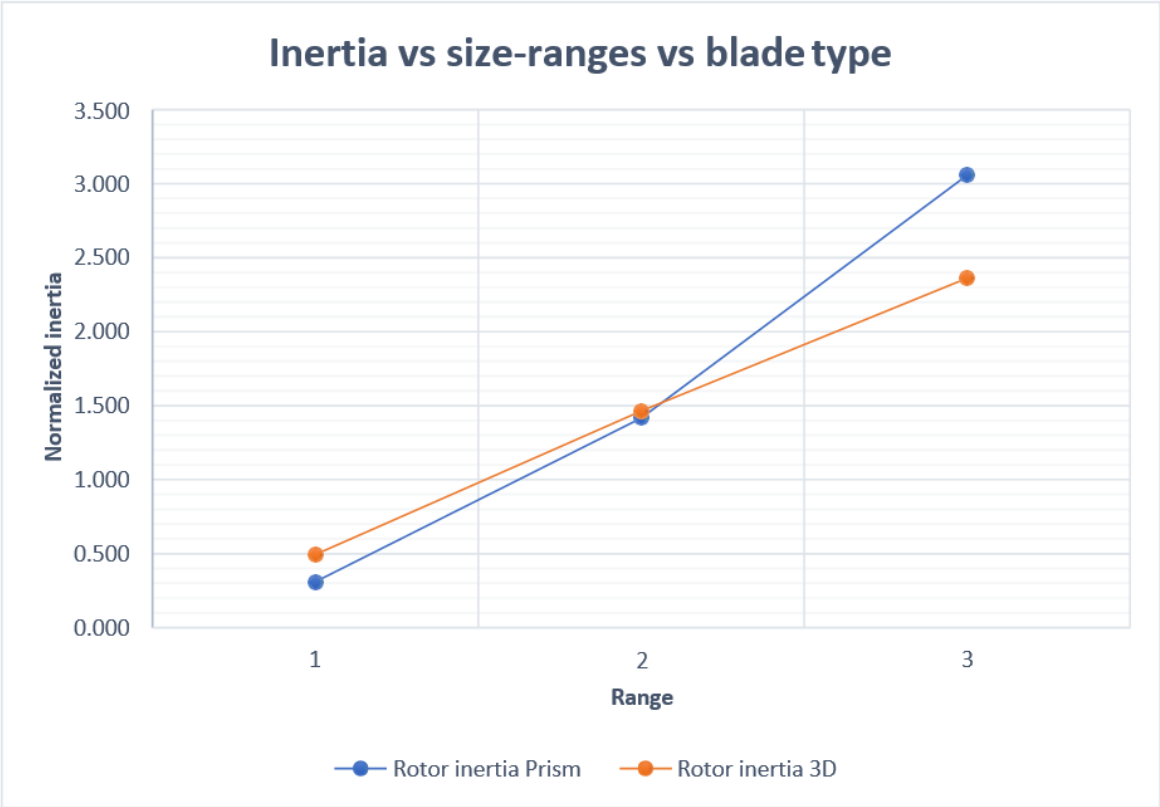

Figure 22. Inertia vs. size ranges and blade types.

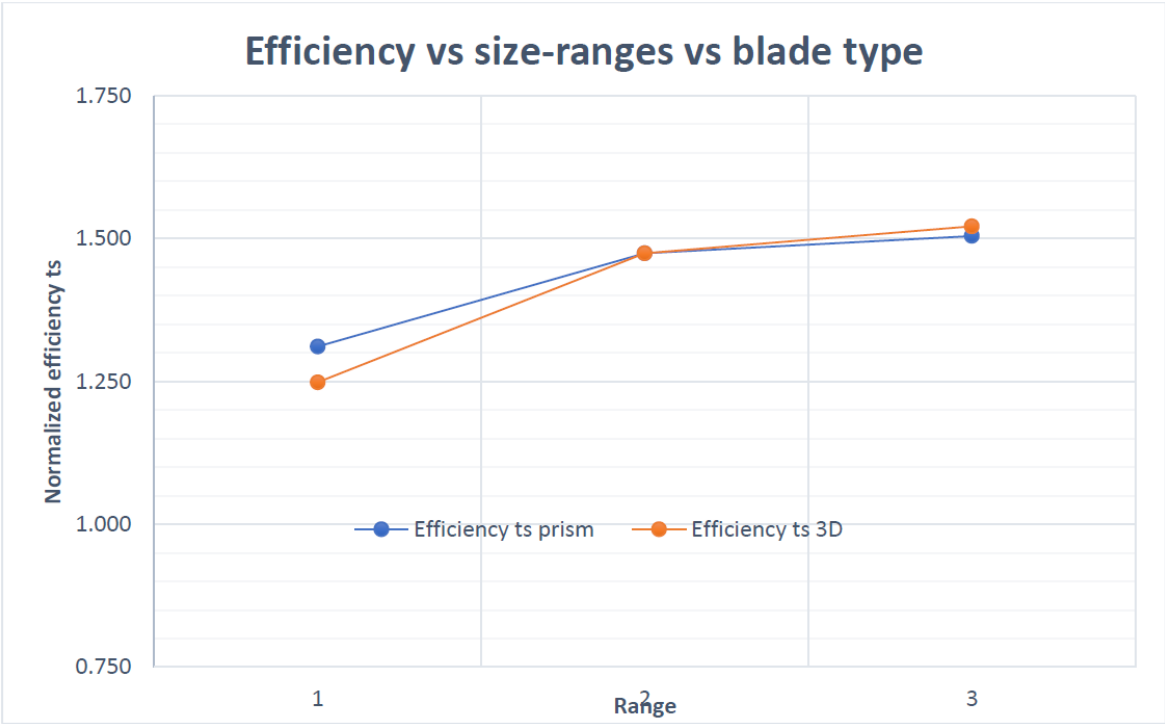

Figure 23. Efficiency vs. size ranges and blade types.

It was believed that the efficiency must also have an influence on the spool-up time, as for the same flow conditions, a more efficient turbine is by definition able to extract more power, or in other words, is able to increase its rotational speed faster, as demonstrated in the following calculations,

where a parameter to better evaluate the performance of the overall spool-up time of the preoptimized turbines was defined.

The mechanical power of the turbine is

$$\dot{W}_{mech} = T \cdot \omega = I\omega^2 \cdot \omega \tag{7}$$

while the efficiency can be expressed as the ratio between the power actually generated by the turbine and the maximum power that can theoretically be extracted from the fluid:

$$\varepsilon = \frac{\dot{W}_{mech}}{\dot{W}_{ideal}} = \frac{I\omega^3}{\dot{W}_{ideal}} \tag{8}$$

From which:

$$\dot{W}_{ideal} = \frac{I\omega^3}{\varepsilon} = P \tag{9}$$

where P represents the maximum power that an ideal turbine working at set conditions can ideally extract from the fluid $\left(\dot{m}\, c_p\, \Delta T\right)$.

Increasing the rpm from $\omega 1$ to $\omega 2$, using $\omega 1 \rightarrow \omega 2$ to study a small transient step, it is possible to write the equation as

$$\frac{I\omega_2^3}{\varepsilon} = P + \Delta P \tag{10}$$

then differentiating considering

$$\omega_2 = \omega_1 + d\omega \tag{11}$$

$$\frac{I(\omega_1 + d\omega)^3}{\varepsilon} = \frac{I\left(\omega_1^3 + d\omega^3 + 3\omega_1^2 d\omega + 3\omega_1 d\omega^2\right)}{\varepsilon} = P + dP \tag{12}$$

and using a first-order approximation valid for small changes in rotational speed

$$\frac{I\left(\omega_1^3 + 3\omega_1^2 d\omega + 3\omega_1\right)}{\varepsilon} = P + dP \tag{13}$$

and eliminating the identity $\frac{I\omega^3}{\varepsilon} = P$

$$\frac{d\omega}{dP} = \frac{\varepsilon}{3\omega_1^2 I} \tag{14}$$

with ε depending on the operating point of the turbine (MFR, P, T, ω).

For simplicity of reference, dω/dP will be called the "spool-up factor".

This relation demonstrates the importance of the ratio between the efficiency and the turbocharger rotor's complete inertia, as it is an important and more comprehensive indicator of the capacity of the turbine to use the exhaust gas energy to spool up the rotor for a given operating point.

As a result, while the turbines in the second range were giving performance improvements in the order of a few percentage points compared to the OEM radial turbine, therefore becoming potential design solutions, the solutions in Range 1 were clearly demonstrating even better results (Figure 24).

Despite the evident advantage of the turbines of Range 1, it was decided to evaluate the spool-up factor for the entire turbocharger rotors (i.e., turbine impeller + compressor impeller + shaft) in order to have an accurate prediction of the performance improvement. The results are highlighted in Table 3, showing a 96% higher spool-up factor compared to the OEM turbine for the Range 1 prismatic one. For this reason, it was chosen to finalize the design with the turbines in Range 1.

To conclude this phase, a production cost estimate was made for the OEM turbine and the two Range 1 turbines. This estimate was performed with quotations from a CNC manufacturing company (Weerg). It was decided that the most suitable axial turbine for mass production would be the prismatic one, as suggested before. The results are graphically compared in Figure 25.

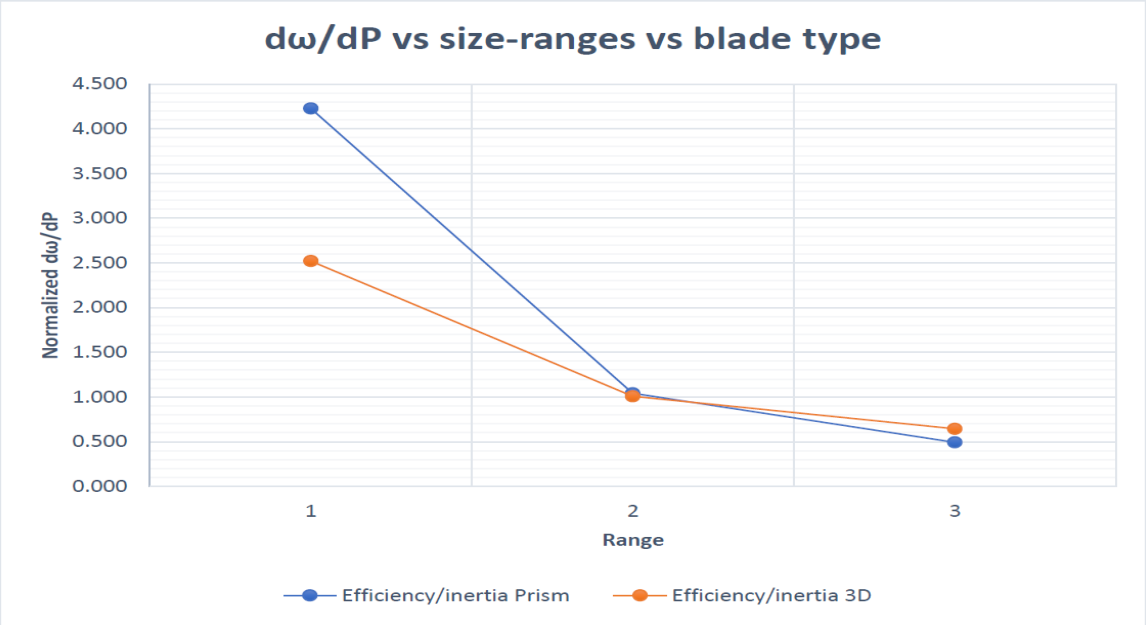

Figure 24. Spool-up factor (dω/dP) vs. size ranges vs. blade type.

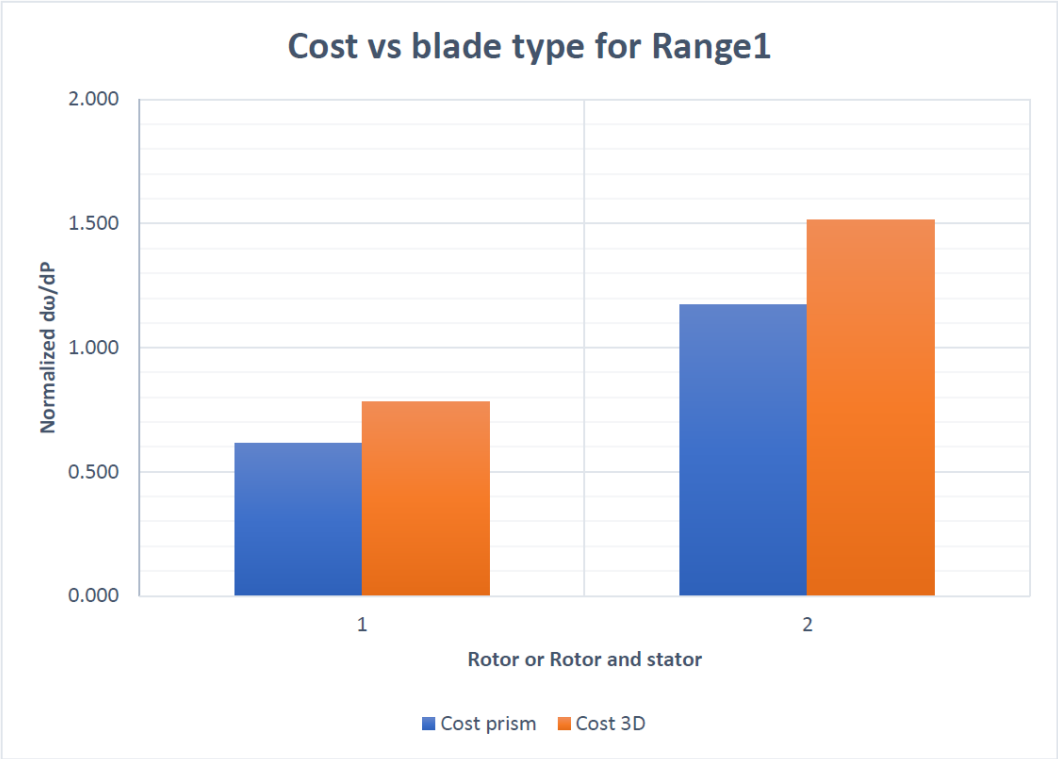

Figure 25. Manufacturing cost of the turbine rotors and rotors plus stators for prismatic vs. 3D blades.

As illustrated by the graph, using rotors and stators, the cost of the prismatic solution would be around 17% higher than the cost of the OEM radial solution. This data represents the cost of the turbine only, that is, not considering the whole turbocharger (compressor, rotor, scrolls, bearings housing, cooling system, wastegate, etc.). Therefore, this difference in cost for the overall final system will be reduced when compared to the cost of the complete system with the other parts. At the same time, it is important to remember the performance benefit of 96% from the turbocharger spool-up time point of

view, in the worst-case scenario (i.e., the cost of the turbocharger does in fact increase by 17% overall) giving a performance-to-cost gain of at least 67.5%.

It is also interesting to observe that using a rotor-only solution (i.e., without stators) would result in a lower cost for the turbine, despite having a plausible loss in efficiency. For this reason, this could be an interesting design to investigate in the future, as the OEM turbine does not have stators as well.

4.2. Profile Optimization

Once the turbine was chosen, a detailed optimization process of the blade airfoil was performed with the method described in the Methodology section.

The DoE optimization generated 20,000 possible airfoil data permutations for the stator and rotor and improved the shape of the airfoil with the aim of reducing profile losses calculated with simplified models accounting for viscosity (Figure 22).

Figures 26 and 27 show the Mach number and Buri criterion distribution along the blade section. These were always checked in such a way to ensure the fulfilling of the Buri criterion and to avoid Mach number values over 1.35, as suggested by [14] in order to limit losses.

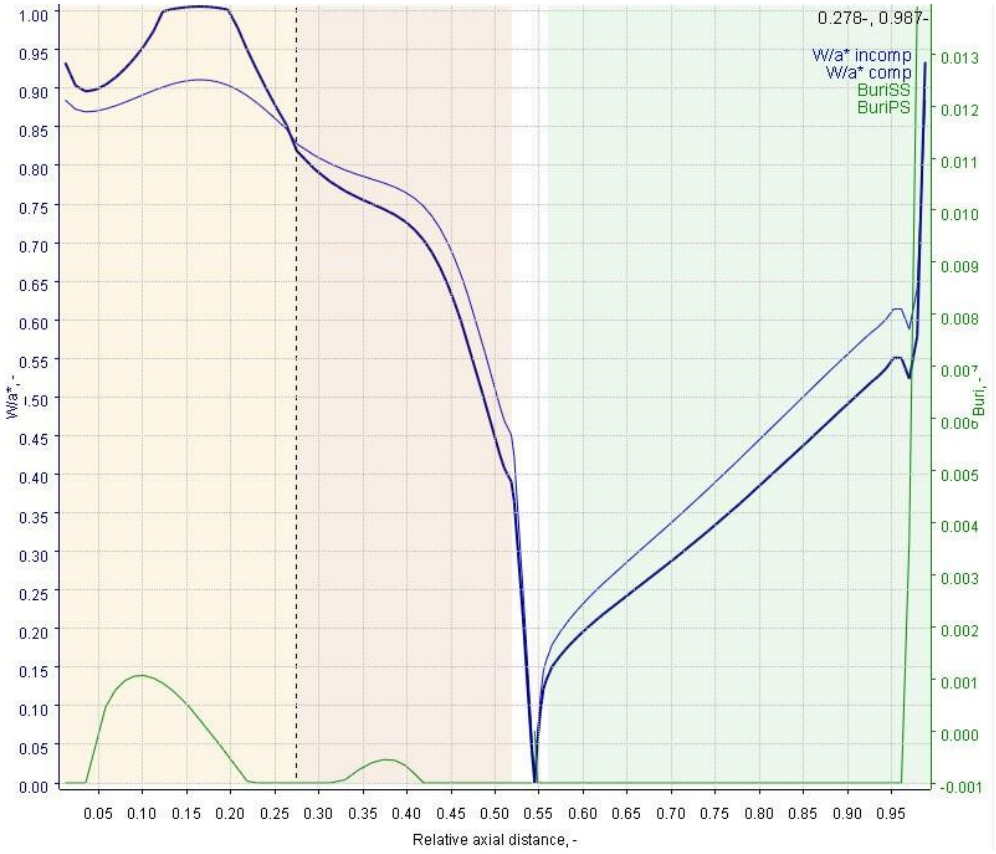

Figure 26. Mach number and Buri criterion plot for the optimized stator airfoil.

It must be pointed out that since the blade is prismatic, it was decided to optimize the middle blade section airfoil, as being in between the hub and tip, it seemed to be a reasonable choice to avoid high differences in loss factors spanwise.

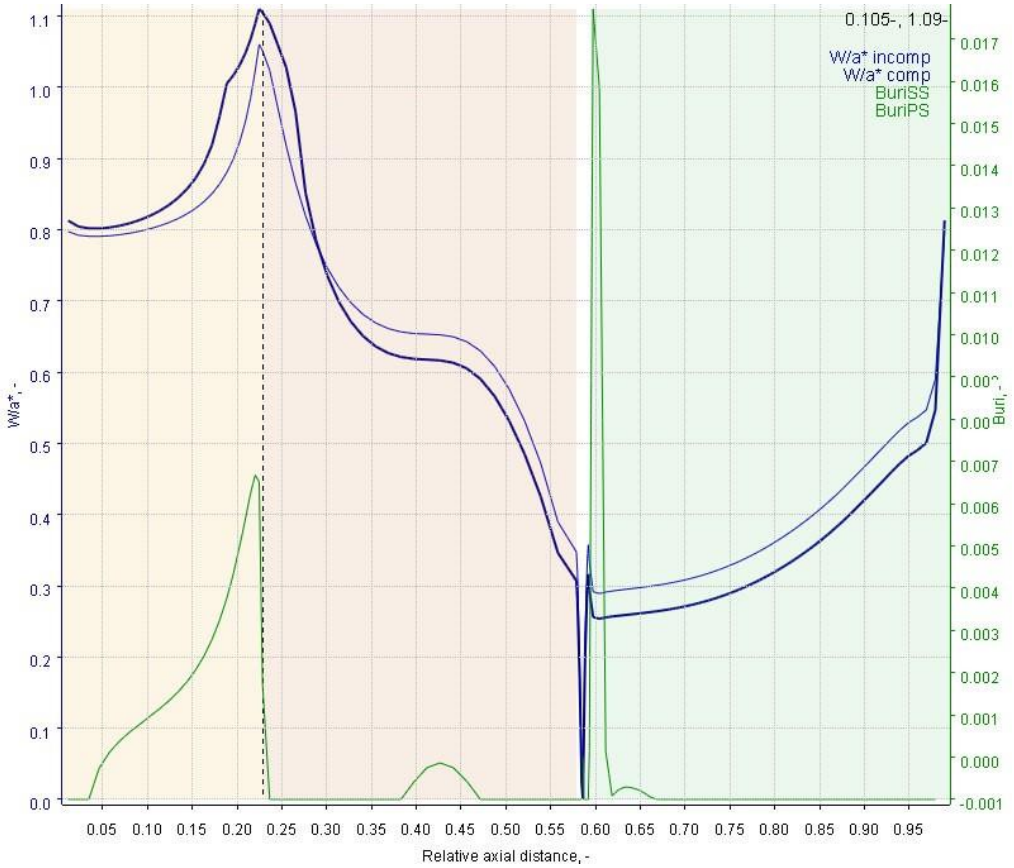

Figure 27. Mach number and Buri criterion plot for the optimized rotor airfoil.

The optimized stator and rotor airfoils are shown in Figure 28.

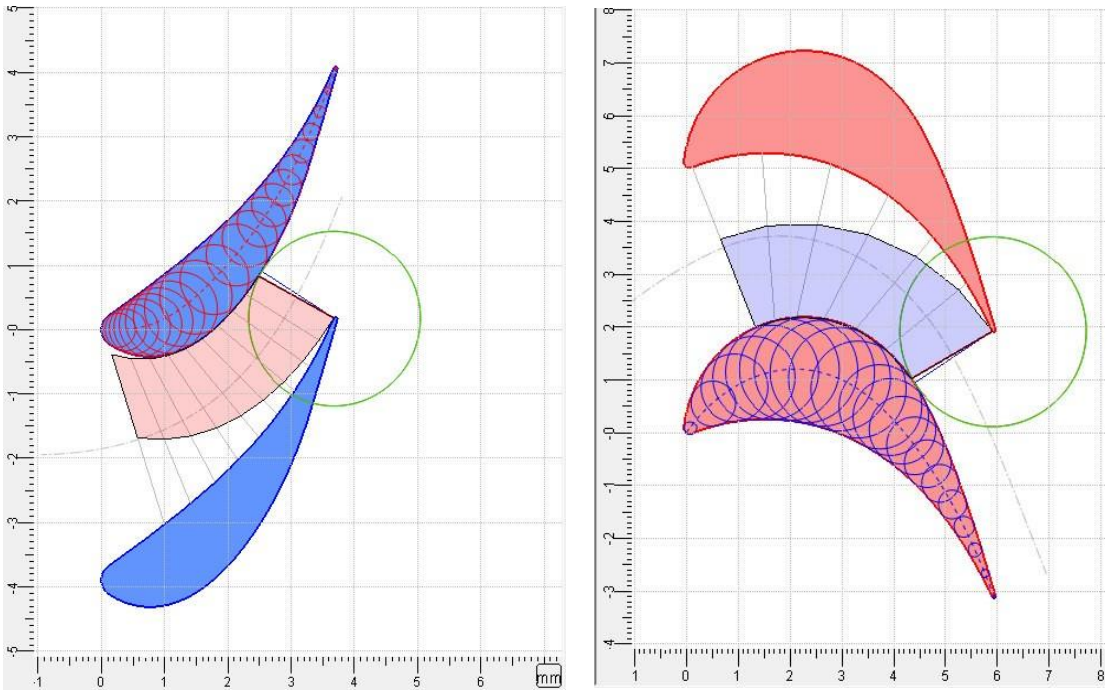

Figure 28. Stator (blue) and rotor (red) optimized airfoils.

The airfoils were than verified via 2D cascade CFD for middle, tip and hub sections in order to check the flow parameters. The following CFD scenes highlight the most interesting results.

Figure 29 shows the result of the central section where the flow is attached until the end of the blade suction side.

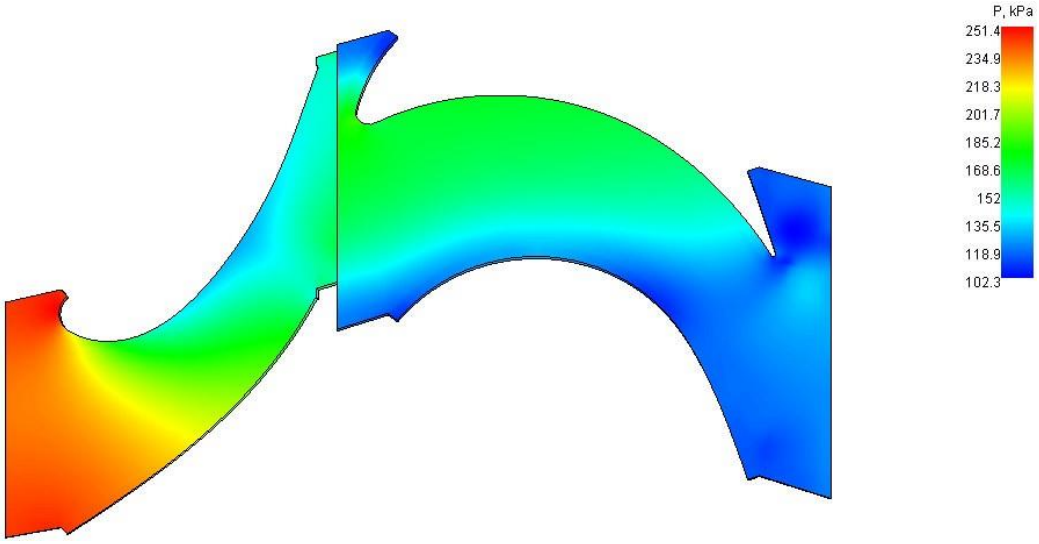

Figure 29. Pressure contours for the middle section of the rotor blade.

On the contrary, Figures 30 and 31 illustrate an interesting phenomenon which intensifies trailing edge losses. In fact, as described, two shockwaves occur at the rotor trailing edge (highlighted in the Mach and pressure scenes) with a recirculating separated flow (clearly visible in the turbulent kinetic energy scene). Despite this, the flow appears attached, ensuring the overall effectiveness of the airfoil in the hub zone.

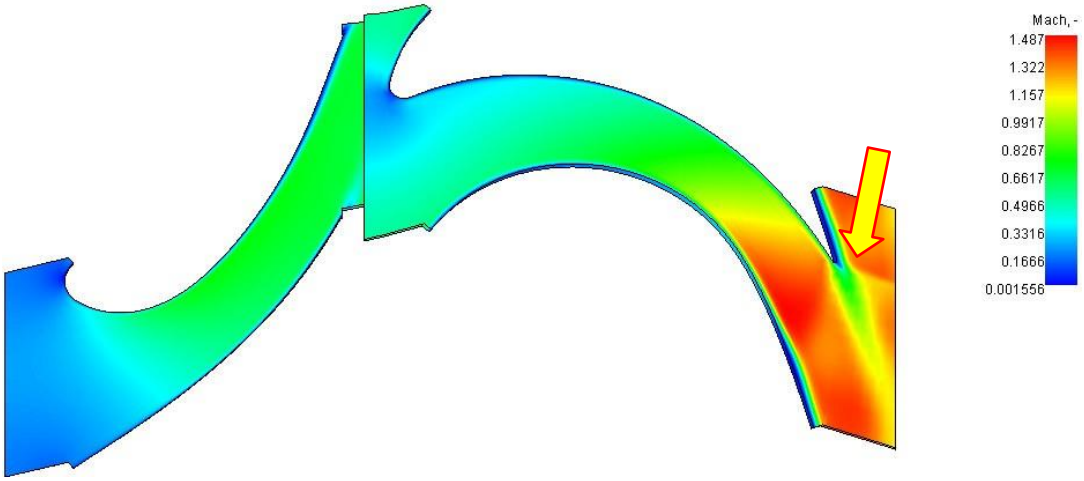

Figure 30. Mach number contours for the 28% spanwise section of the turbine.

Near the tip, the flow is attached until around 80%, and then appears to stall in the unguided turning zone next to the trailing edge, suggesting possible higher tip losses, as shown by the entropy plot (Figure 32). However, as these are 2D cascade CFD simulations and the flow is expected to have a strong 3D behavior near the tip because of tip leakage and the higher angular velocity of the rotor, it was decided to continue with the developed airfoil with more accurate CFD analysis.

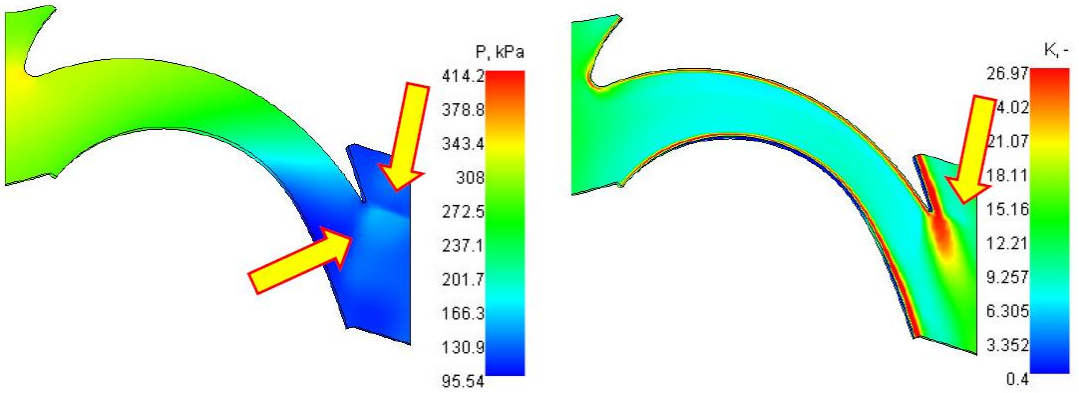

Figure 31. Pressure (**left**) and turbulent kinetic energy (**right**) contour details of the rotor blade (28% spanwise).

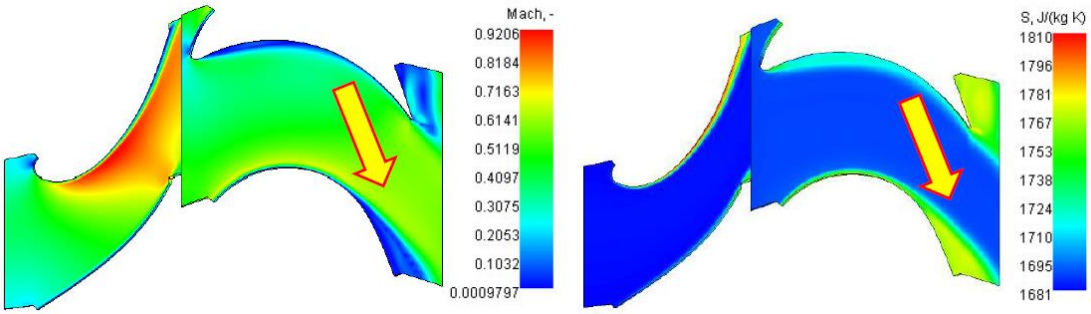

Figure 32. Mach number and entropy contours (85% spanwise).

4.3. Detailed 3D CFD Simulation

Finally, detailed 3D CFD simulations were performed again for every 1000 engine rpm interval, replicating the tests conducted with the axisymmetric method with 3D periodic simulations.

The fluid domain mesh described in the Methodology section is shown in Figure 14 and in more in detail in the following Figure 33, where the O grid around the airfoil surface, the tip clearance hexahedral mesh and the leading and trailing edges' mesh refinements (performed to catch eventual separation bubbles or separated areas) are evident.

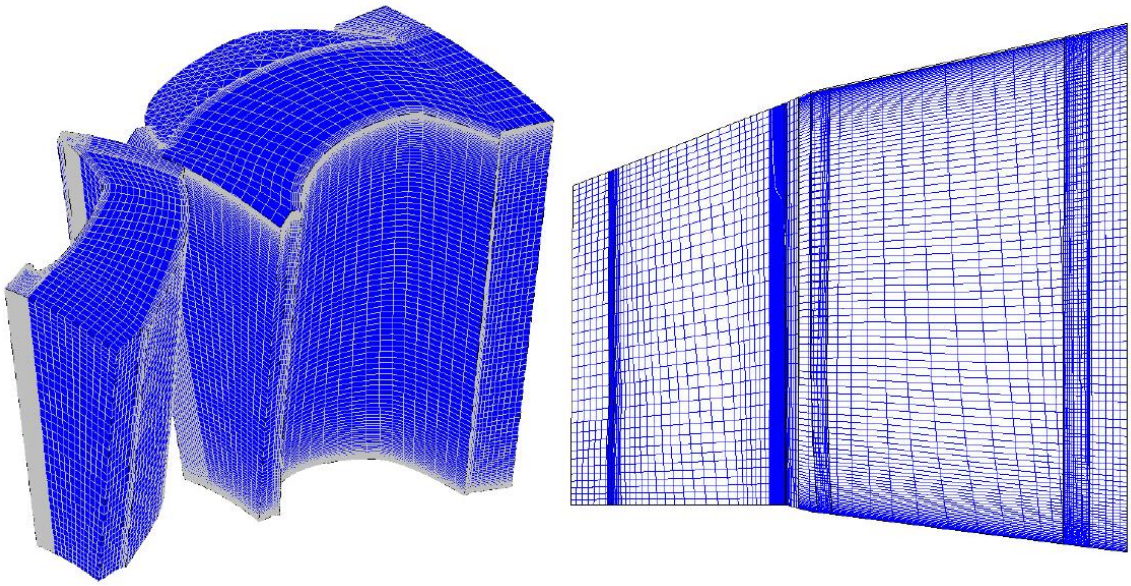

Figure 33. 3D CFD mesh details.

The 3D simulations confirmed the results obtained via streamline analysis and axisymmetric CFD, especially regarding the turbine power (Figure 34) and spool-up factor (Figure 35), as shown in the following plots. As the pure performance results are the same as the axisymmetric simulations, the same considerations are valid and are not repeated in this section.

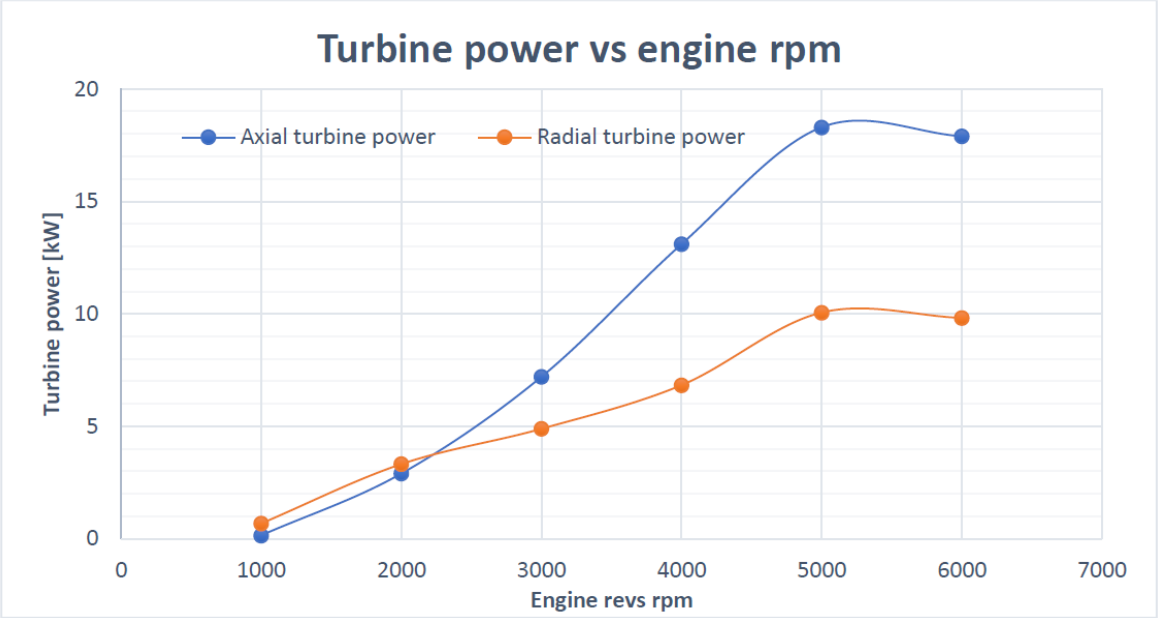

Figure 34. Comparison of generated power for the proposed axial turbine and the OEM radial turbine (3D CFD).

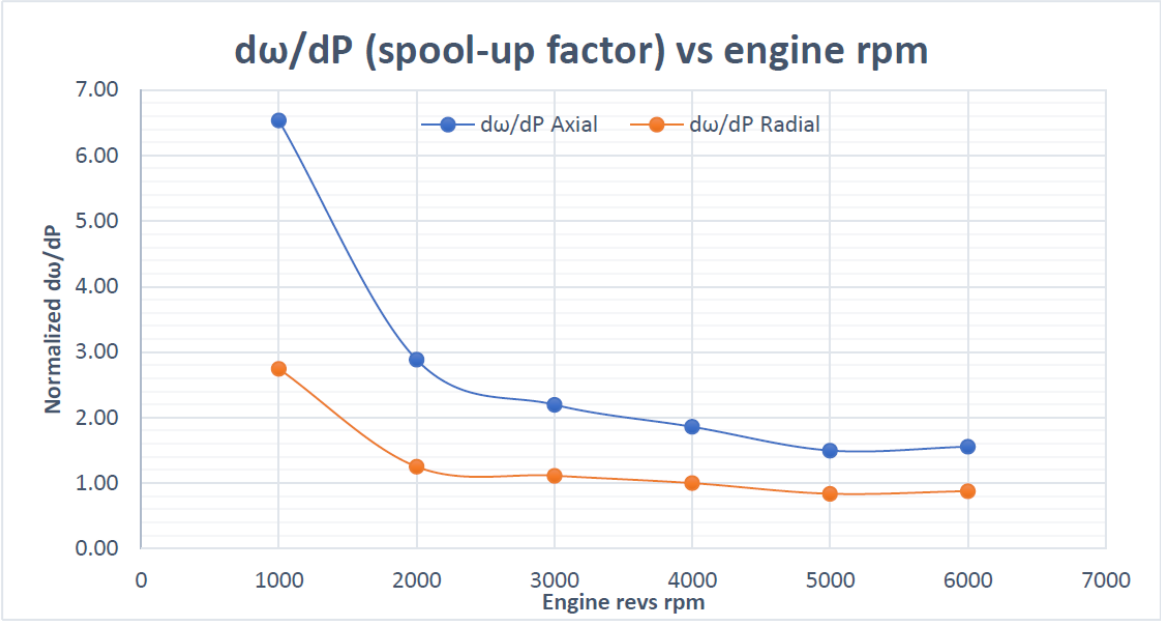

Figure 35. Comparison of the spool-up factor for the proposed axial turbine and OEM radial turbine (3D CFD).

In the above graph, the good correlation with the previous axisymmetric simulation is evident.

As this work showed that for low aspect ratio blades, a prismatic blade could perform very well for these flow conditions, it will be interesting to examine the 3D flow in detail to investigate where the main losses come from.

With a fairly good correlation with the 2D cascade simulations, the flow appears attached span wise, despite a few differences (Figure 36). In fact, at the hub section, a separation bubble (Figure 37) at the blade leading edge causes the transition to a turbulent boundary layer, which was not shown in the 2D simulation. As expected, the entropy graph shows good correlation with the literature and 2D cascade CFDs, as it shows the secondary and trailing edge losses' effect in the area.

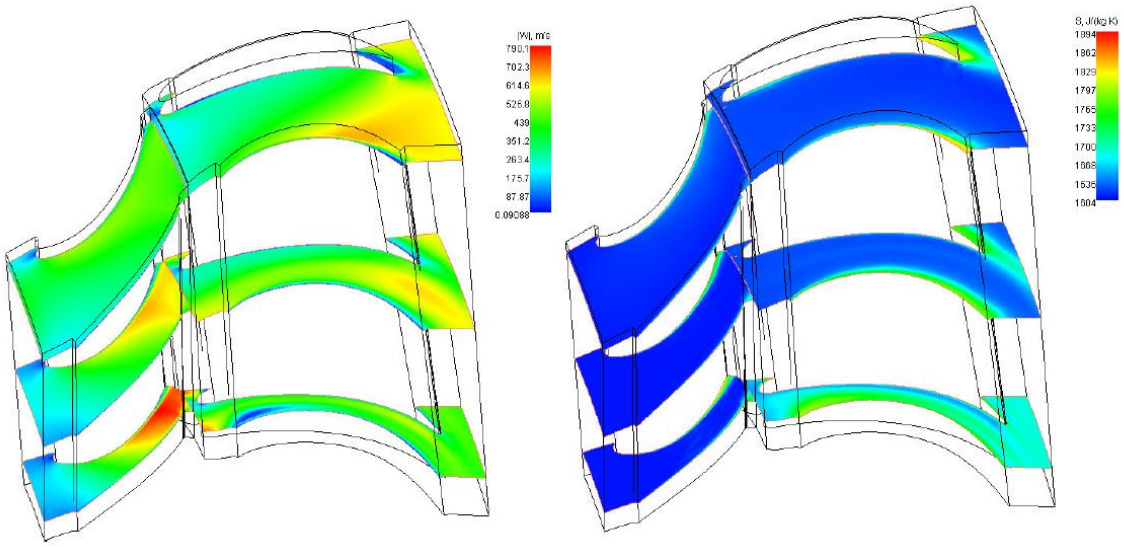

Figure 36. Velocity and entropy contours at the design point.

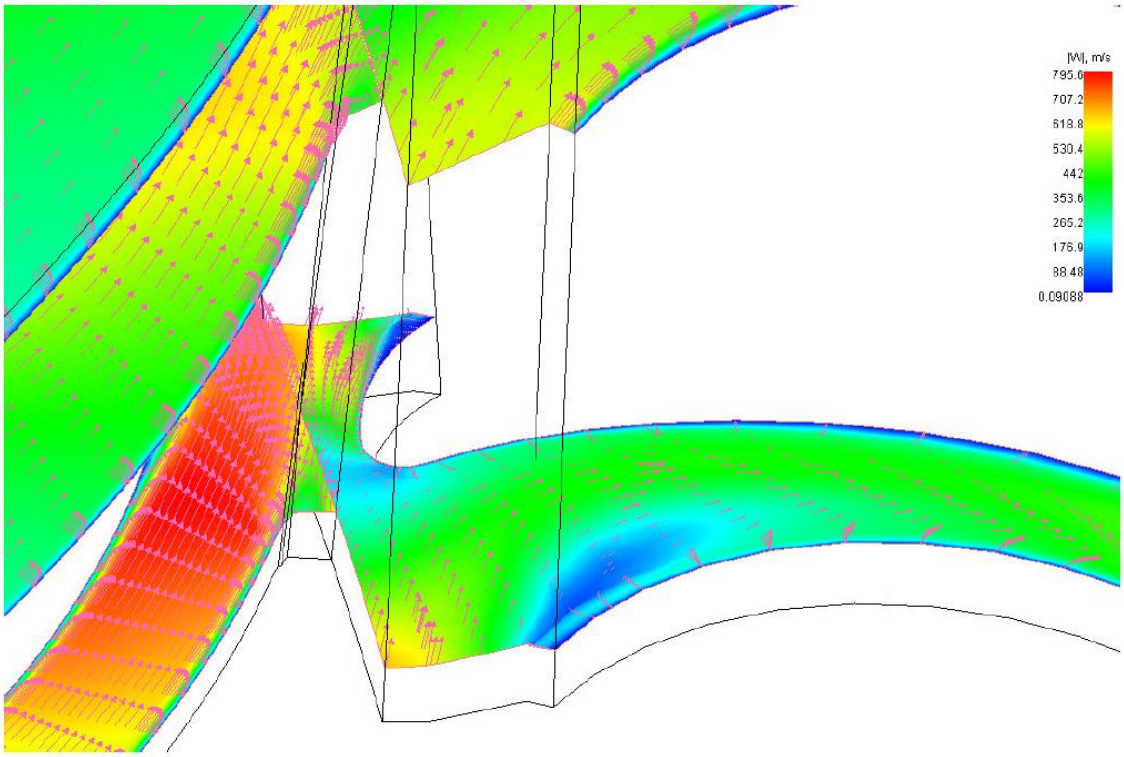

Figure 37. Velocity and velocity vector details of the hub section of the rotor highlight the separation bubble.

Further, at the tip section, the flow is more attached than that shown in the 2D cascade CFD. However, a difference was expected in this area due to the more three-dimensional nature of the flow. Nevertheless, it is interesting to note an increase in entropy next to the tip, which will be discussed later.

Consistent with the literature, secondary losses due to the turbulence generated next to the hub and casing walls are visible in red in Figure 38. Figure 39 further highlights this phenomenon, showing the increase in entropy, and therefore the increase in losses, as suggested by the interpretation proposed by [15], in the right-hand side of the image next to the hub.

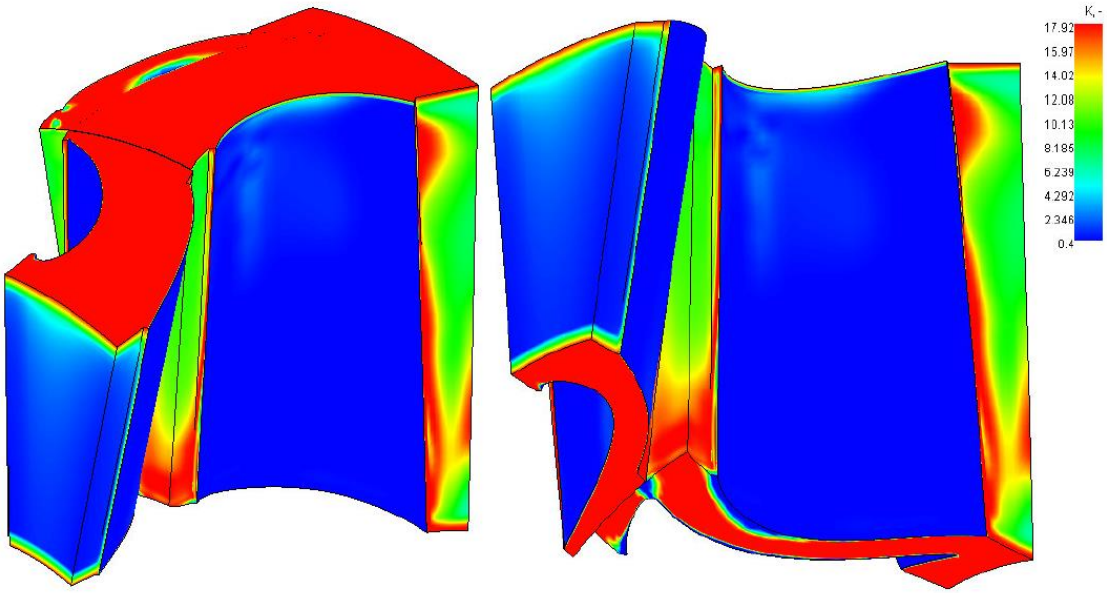

Figure 38. Wall surface turbulent kinetic energy scenes.

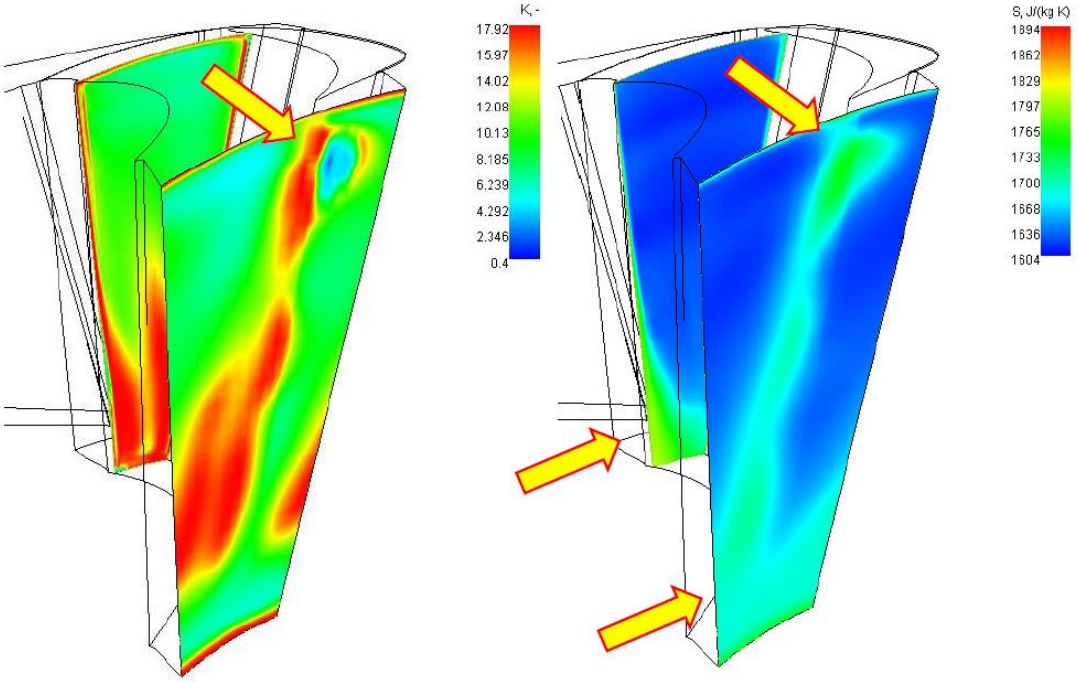

Figure 39. Turbulent kinetic energy and entropy streamwise section scenes.

Moreover, in the same image, evident from both the turbulent kinetic energy and from the entropy scenes is a tip leakage flow that develops a strong tip vortex, therefore strongly contributing to the tip leakage losses.

Despite an overall good aerodynamic behavior of the blade, the shear flow bubble at the hub section leading edge and the strong tip vortex at the blade tip must be accepted as a compromise to reduce production costs compared to a more optimized 3D blade.

4.4. FEA Analysis

As discussed in the Methodology section, different materials were chosen for the rotor and stator blades as the rotor spins at very high speeds, therefore generating potentially critical centrifugal loads. For this reason, great attention will be given to the analysis of the rotor in respect to the stator, as the latter does not experience centrifugal loads and its blades are structurally constrained at both the hub and tip sections.

As AxFEA did not allow for the required highly controlled and structured mesh, it was decided to simulate the rotor in ANSYS using the loads from the CFD simulation in a simplified manner (i.e., equally distributed forces on the blade suction and pressure sides + simple uniform thermal load and centrifugal forces).

It was important to have proper control of such structurally critical section of the blades, as the root area presents many relatively sharp edges, which can pose issues in solving the problem with values outside the elastic range. The type of mesh used is made of tetrahedral elements, in contrast to that suggested in AxFEA (made of cubic elements in the blade zone and tetrahedral ones in the hub and tip areas), and has strong control on the mesh quality and sizing, especially in the blade and root areas. In fact, as is visible in Figures 40 and 41, the mesh was kept finer in the blades and especially on the surface, as they are the areas with higher bending stress, and even finer at the blades' root, as the centrifugal and bending stress are maximal in those areas.

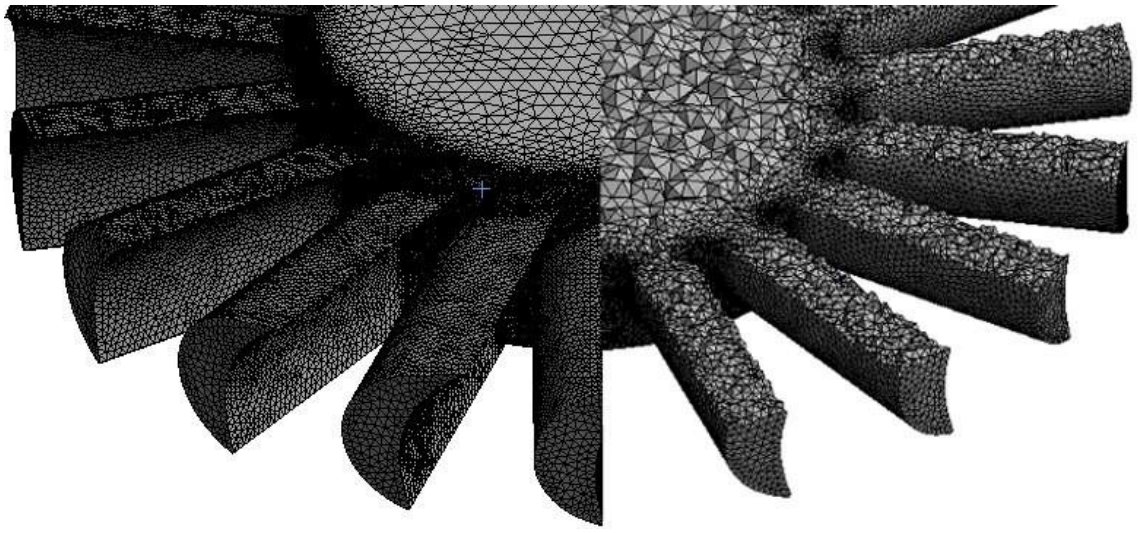

Figure 40. Surface (**left**) and section view (**right**) of the rotor mesh illustrates the elements' size and distribution.

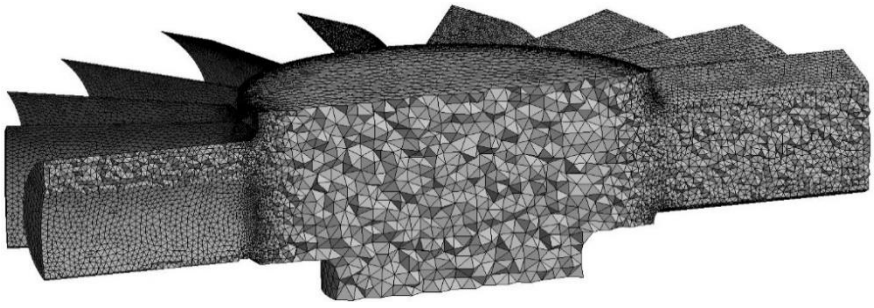

Figure 41. Axial rotor mesh section view.

Analyzing the results of the simulation, keeping in mind that the short-duration maximum allowable stress of the material is 950 MPa at the maximum flow temperature, and that in reality the rotor will be colder as it is liquid-cooled at the shaft, the final simulation results are positive and

in agreement with the preliminary structural calculations performed during the predesign phase (Figures 42 and 43).

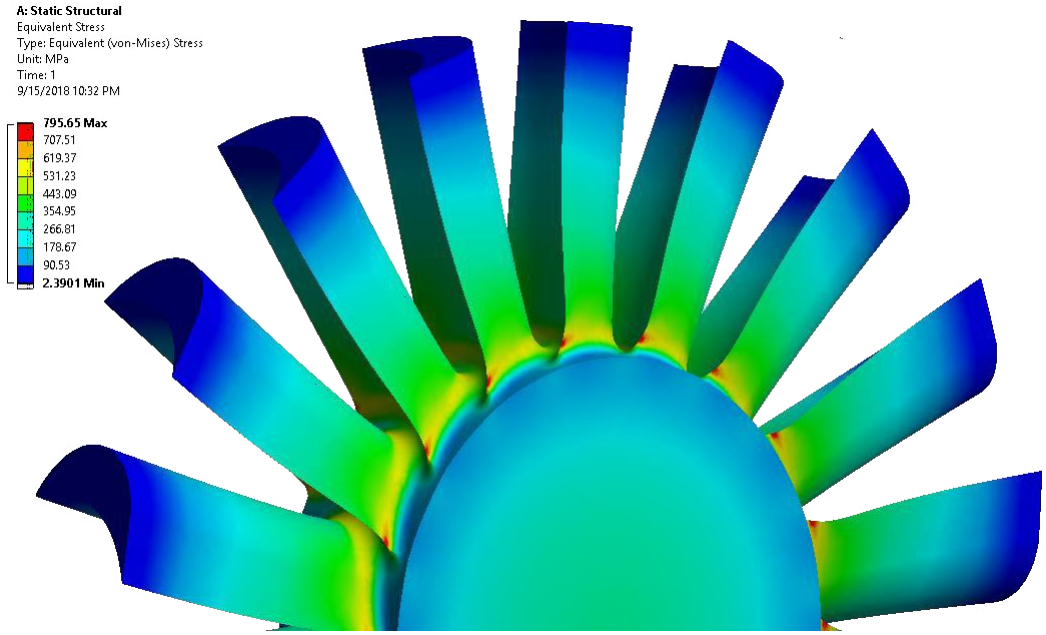

Figure 42. Rear view of rotor surface stress (von Mises).

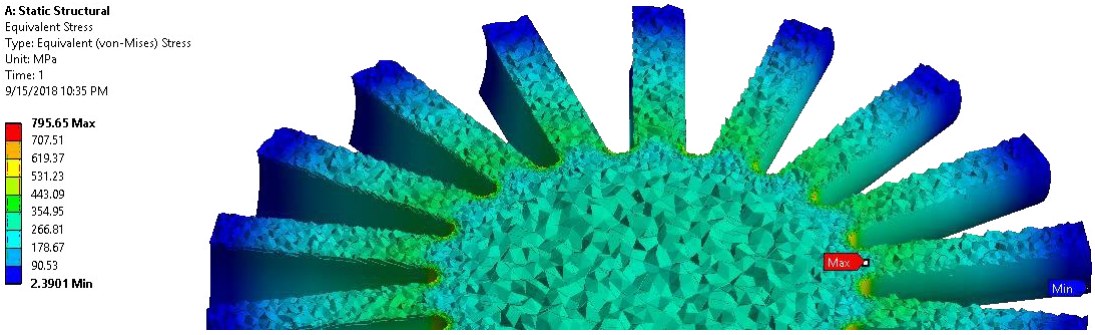

Figure 43. Rotor stress section view (von Mises).

It is important, however, to take into account the long-duration resistance of the rotor, as it is not made for motorsport applications and durability must be considered. The material data shows that relevant creep problems may arise after at least 1000 h of continuous loading at that temperature, which is reached at 6000 rpm with full load, with a reduction of the allowable maximum stress to 670 MPa. At this condition, with a vehicle speed of 180 km/h, and it seems unreasonable to design the blade to withstand those critical conditions for 1000 h of continuous operation.

Apart from certain small areas, as shown Figure 43, most of the elements show a stress level under 670 MPa, therefore potentially enduring 1000 h of continuous critical operativity. The elements displaying higher stress are carefully analyzed in the following paragraphs.

As shown in Figure 44, the critical areas of the simulation are in the airfoil trailing edge area on the root. Since the yellow and most of the orange-colored elements are within the acceptable long-duration stress limit, the only problem may be in the red areas, showing values up to 795 MPa. In reality, it is important to note that due to the defeaturing algorithm in the masher, a sharp edge is generated in that area, as shown in Figure 45, instead of the designed slightly smoothed corner illustrated in the profiling section, therefore increasing the local stress more than what could plausibly be expected. As a

further demonstration, a rapid stress drop into the acceptable values of von Mises stress levels is clear from Figure 44 next to the trailing edge of the blades, just one series of nodes inside the blade.

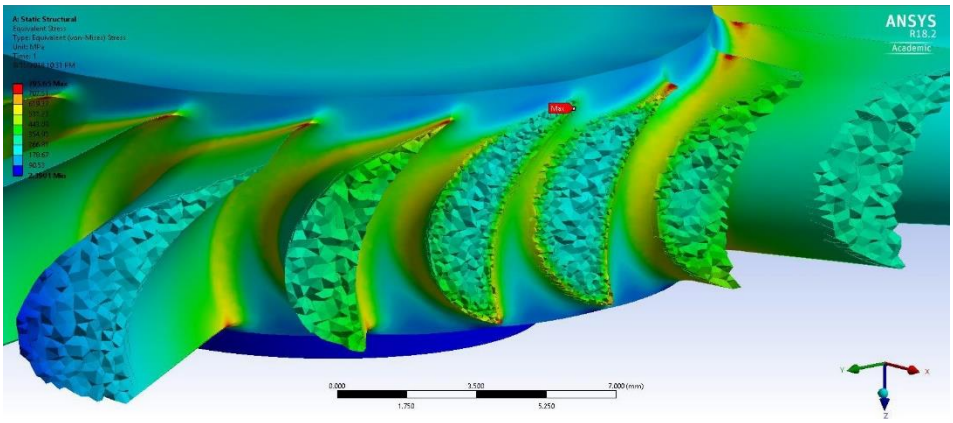

Figure 44. Blade root stress sections.

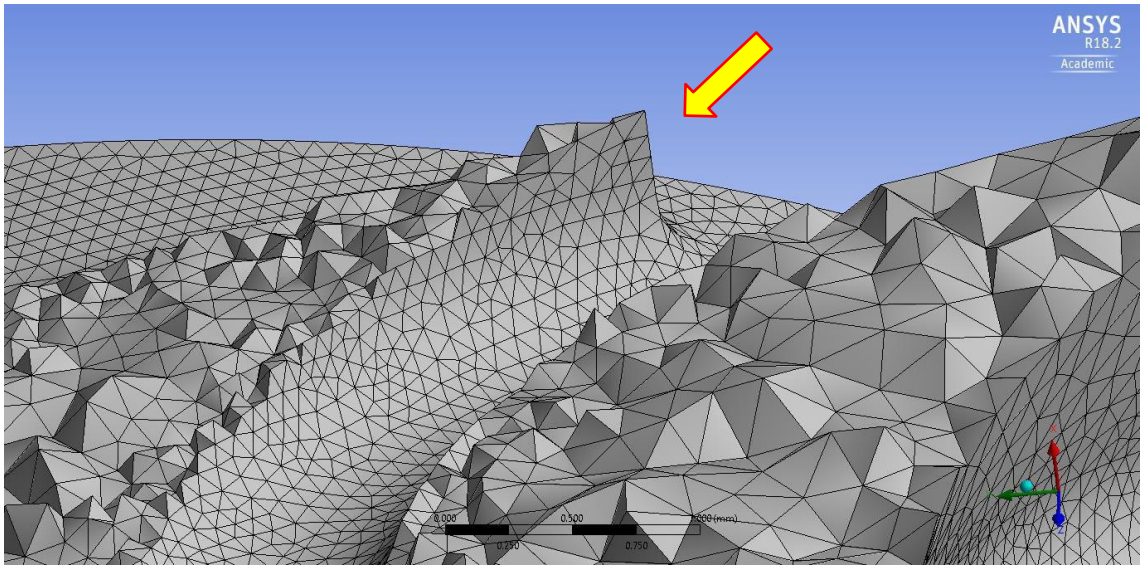

Figure 45. Blade root trailing edge mesh detail (section).

To conclude, short-duration operativity typical of normal driving conditions was confirmed with an average safety factor of 6.57. Further, with the discussed consideration, the suitability of the designed blade rotor was demonstrated for the most critical operative conditions for 1000 h of continuous operativity, despite a smaller average safety factor of 4.64. The structural safety factor data are illustrated in Figure 46.

Regarding the rotor, no issues were highlighted as it is not rotating, and the nozzle blades are fixed at both hub and tip sections. The use of Inconel instead of steel was motivated to avoid creep and oxidation in long-term use.

Note that the higher stress on the shroud elements in Figure 47 is due to two main factors: the no-displacement constraint (in reality, it would be able to dilatate because of the temperature at a rate similar to that of the casing), and the shroud being less thick than the chosen one illustrated in the next paragraph, due to the software settings. The stress is nevertheless less than the limit at maximum temperature. Further, this side of the shroud is not exposed to the flow, and thus being at an even cooler temperature, it would be significantly stronger than the blade.

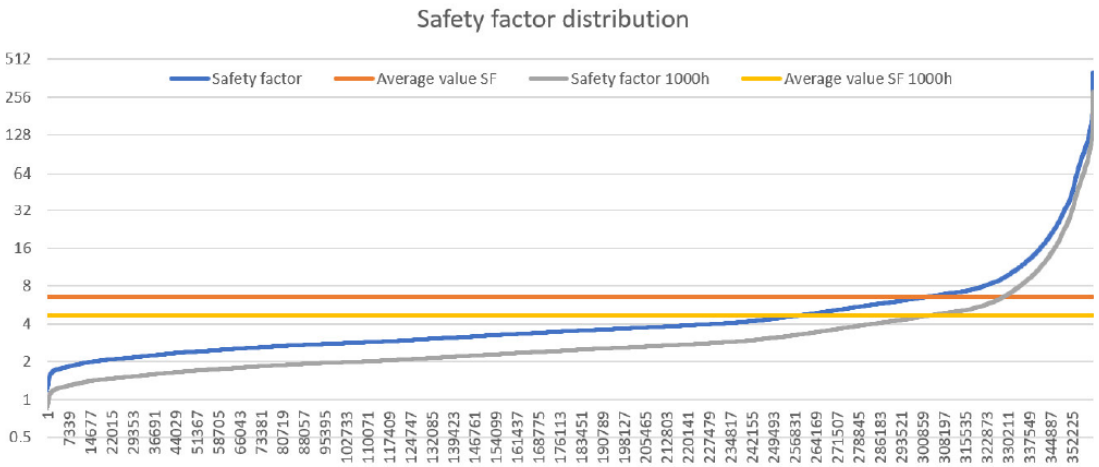

Figure 46. Safety factor (SF) distribution calculated at each mesh node ($\log_2$ scale on the vertical axis).

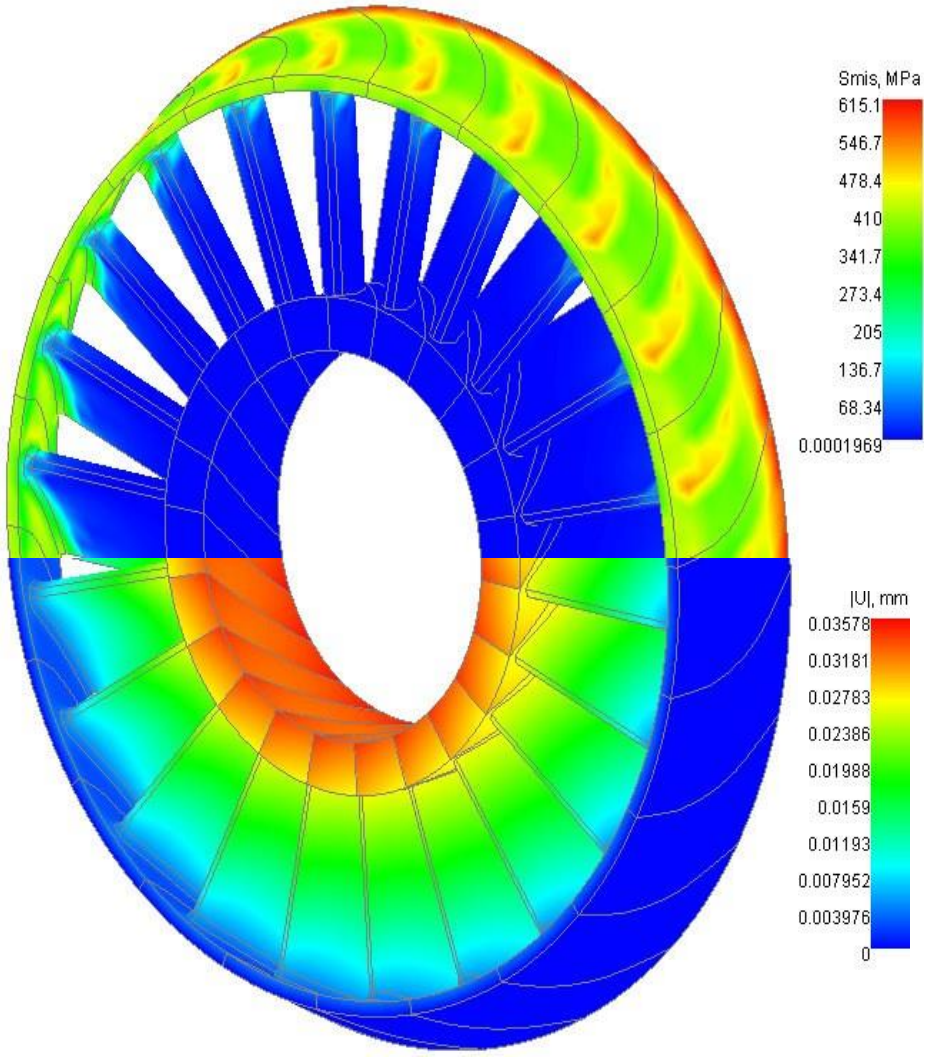

Figure 47. Stator blades' von Mises stress distribution (**top**) and displacement (**bottom**) scenes.

4.5. Final Stator and Rotor Design

The design evolution is shown in Figure 48 (original – OEM – turbine) and the proposed axial design is provided in Figure 49.

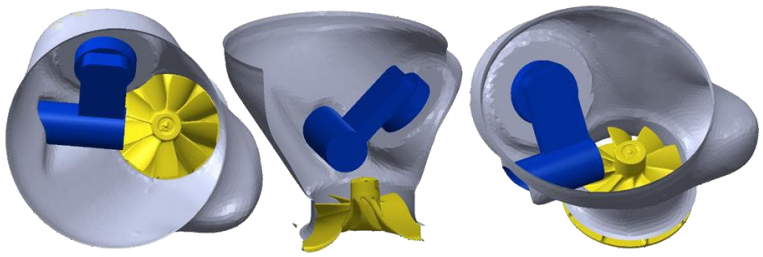

Figure 48. OEM turbine and diffuser (aerodynamic surfaces only) views.

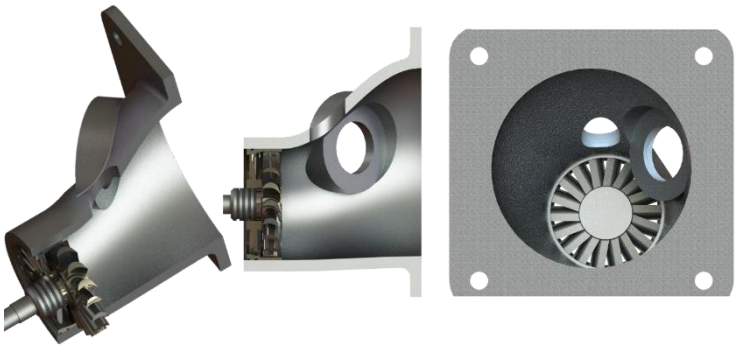

Figure 49. Proposed axial turbine with diffuser.

Another strong point of the proposed solution is its packaging. A layout similar to the OEM one with an almost identical diffuser and the same scroll was obtained, ensuring no changes are required to interface with the original power unit. The exhaust manifold, exhaust pipe and turbocharger bearing housing can be maintained in the same position. As the OEM turbine receives the turbine inlet gas radially contraposed to the axial one, for the proposed solution, it is necessary to change the flow direction with a couple of aerodynamic "adapters", as illustrated in red and yellow in Figure 50. In the picture, the scroll is identical to that of the OEM turbochargers.

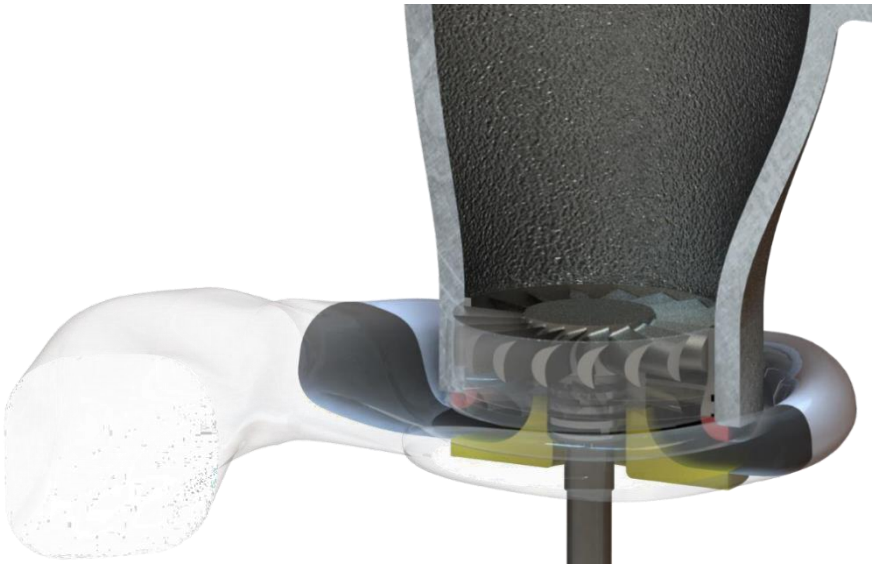

Figure 50. Axial turbine assembly concept with OEM scroll (inner surface only) and aerodynamic adapters.

4.6. Electric MGU Coupling

As the turbine produces more power than what is required by the compressor, an electric motor-generator unit or an alternator could potentially be mounted on the turbocharger (Figure 51) axis, similarly to what is already done in Formula (1). This feature would permit one to exploit the turbine excess power in a useful manner, charging the vehicle batteries when activated in generator mode, therefore potentially allowing the removal of the crankshaft-attached alternator that "removes" power from the transmission, increasing the efficiency of the power unit and the power delivered to the wheels. Further, when active in generator mode (in the motor/MGU case), it can help to spool up the turbocharger even faster than what is already achieved by the implementation of the axial turbine. In the case of using an alternator instead of an MGU, a clutch must be used in order to decouple the generator from the turbocharger to reduce the spool-up time (for example in sport mode or for urban driving).

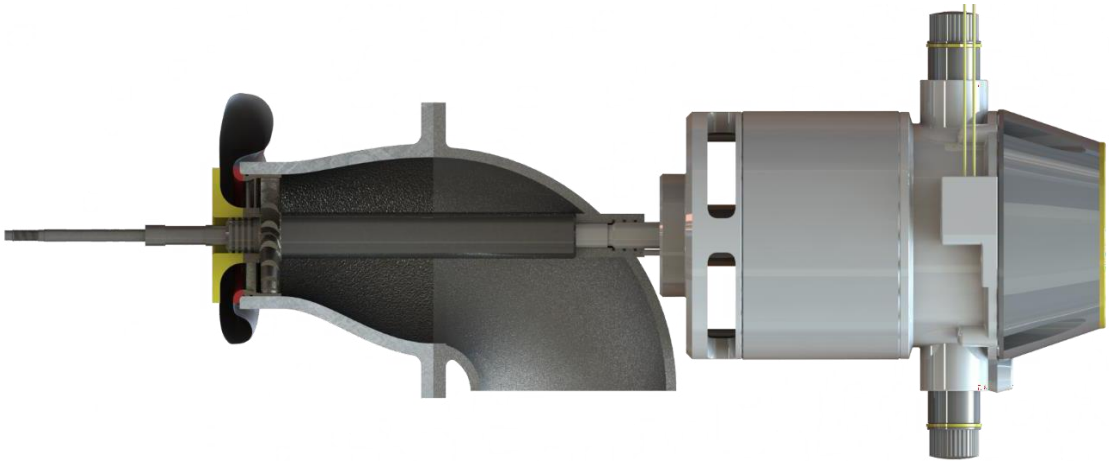

Figure 51. Concept of the turbine and Motor Generator Unit (MGU) layout.

As the original alternator is a 14 V 150 A electric generator, it should produce $P = RI = 2100$ W at max regime. Checking the turbine power plots, the axial turbine would produce 2.1 kW of extra power at only 3000 engine revs.

Regarding Figure 51, it is common to mount the MGU on the compressor side, as this maintains it at lower temperatures because of the increased distance from the hot side. However, in this case, this would mean changing the compressor-to-turbine connecting shaft to withstand more torque, therefore necessitating the redesign of the entire housing and turbocharger.

4.7. Proposed Manufacturing Methods

The turbine rotor is proposed to be manufactured using Inconel-738 material via casting and CNC machining, and eventually a plasma-sprayed ceramic coating to increase the operating life and reduce the heat transfer inside the blade. Radial molds can be used to have a preliminary cast of the blade shape, reducing the CNC machining efforts and potentially allowing for directional solidification, increasing the turbine blades' strength in the radial direction [16].

The turbine shaft is proposed to be manufactured using steel and machining on a lathe and friction steer welded to the turbine rotor.

The stator nozzles are proposed to be manufactured using Inconel-738 material via casting and CNC machining, and eventually a plasma-sprayed ceramic coating to increase the operating life. Similarly to the rotor, radial molds can be used.

The stator shroud is proposed to be manufactured using Inconel-738 material, by extruding a tube machined on the lathe for accurate tolerance, then electrical resistance welded (ERW) to the nozzles, as shown in Figure 52.

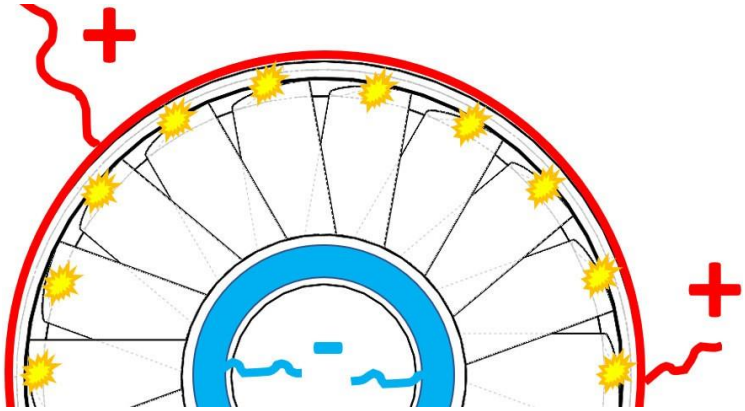

Figure 52. Electrical resistance welding (ERW) concept for production cost savings for the stators (red/blue—electrodes): to be simulated.

The diffuser and scroll are to be manufactured using stainless steel by casting and machining of low-tolerance areas.

5. Conclusions

Initially, 3D optical scans were performed, which allowed the proper measurement of the properties of the OEM turbocharger, such as the rotational moment of inertia of the turbine, compressor and shaft, and to use much of this data as references for the mechanical design of the axial turbine. A dyno-calibrated 1D Ricardo-Wave engine model (Ford EcoBoost 1.0 L) was used to calculate the aerothermal boundary conditions for the design of the turbine at every interval of 1000 rpm from 1000 to 6000 rpm to have all the required boundary conditions data to design/test the turbine at different engine operating points.

The initial idea of low-aspect-ratio prismatic blades having similar efficiency to 3D twisted blades was tested via thermodynamic calculations and streamline optimization and then verified. Many turbines of several size ranges and different blade types (prismatic vs. 3D twisted) were predesigned at 2000 and 4000 engine rpm (full load) operating points, mapped and compared to check the suitability for the engine and compressor requirements. After choosing the final design, it has been simulated by means of increasing-precision CFD RANS analysis, including 2D cascades for airfoil profile optimization, axisymmetric simulations and full 3D simulations. FEA analysis concluded the turbine design phase, as this validated the preliminary structural calculations performed in the preliminary design phase.

The spool-up performance of the proposed axial turbine was found to be up to 2.67 times higher than the OEM radial one. The power output of the axial turbine was comparable to that of the original radial one for lower engine rpm values (<2000 rpm) and was significantly greater for higher engine revs, therefore potentially allowing for the implementation of an electric MGU to further increase the power unit efficiency, and potential removal of the crankshaft-connected alternator.

The proposed solution showed a cost increase by 17% for the turbine part only (radial rotor vs. axial stator + rotor). This cost rise could be reduced with intelligent manufacturing methods, and in any case, does not represent an overall increase in the turbocharger cost by the same amount, as that cost of all the other parts would negate such an increase. Further, it was demonstrated that the proposed design can be fitted on the engine of choice without any interface change, which helps to mitigate the increase in the cost of the vehicle, particularly when considering the resultant performance increase as well.

Author Contributions: L.B. and M.A. were the research students who conducted the project at Brunel University London. A.P. is the turbomachinery group leader in the Centre of Advanced Powertrains and Fuels (CAPF) at Brunel University London, who conceived of the project, the layout of the investigations and checked the

computational outcome of the resultant modelling effort and subsequent discussion while D.G. provided control and draft checking and editing as well. All authors have read and agreed to the published version of the manuscript.

Funding: This research has received funding from the Engineering and Physical Sciences Research Council Impact Acceleration Account for the project titled "Axial Turbine Design for Advanced Turbocharger Application" with Brunel University internal CHIME code (11573109).

Conflicts of Interest: The authors declare no conflict of interest.

Nomenclature

OEM	Original Equipment Manufacturer
CAM	Computer Aided Manufacturing
CAE	Computer Aided Engineering
CAD	Computer Aided Designing
CFD	Computational Fluid Dynamics
KPI	Key Performance Indicator
$\frac{d\omega}{dP}$	Spool-up Factor
SLM	Selective Laser Melting
VGT	Variable Geometry Turbine
RPM	Rotations per Minute
I	Moment of Inertia
ρ, rho	Density
l	Turbine Axial Length
r_t	Turbine Tip Radius
r_h	Turbine Hub Radius
U, U_tip	Blade Tangential Velocity (Tip -> At Tip Section)
C_0	Spouting Velocity
$q(s)\perp$	Leaned Blade Shear Load Component Function
$q(s)//$	Leaned Blade Axial Load Component Function
$T(s)$	Leaned Blade Shear Force Function
$M(s)$	Leaned Blade Bending Moment Function
ω	Angular Velocity
s	Bladewise Coordinate
SST	Shear Stress Transport
ECU	Electronic Control Unit
cc	Cubic Centimeters
T	Temperature
$\dot{W}_{mech}$	Mechanical Power
$\dot{W}_{iso}$	Maximum Power for Isentropic Transformation
ε	Thermodynamic Efficiency
Cp	Specific Heat at Constant Pressure
P	Short Notation for $\dot{W}_{Iso}$
R	Generic Radial Coordinate
MGU	Motor Generator Unit (H—Heat, K—Kinetic)
ERW	Electrical Resistance Welding
ṄN_dot	Mass Flow Rate
c_Z	Axial Component of The Fluid Velocity Vector
BSR	Blade Speed Ratio (U/C0)
T_T	Torque, Temperature
P	Pressure
P_T	Total Pressure
h	Enthalpy
h_T	Total Enthalpy
gamma	Specific Heat Ratio

tur_eff_est	Turbine Estimated Efficiency (Based on Literature)
R,*R_spec*	Gas Constant, Specific Gas Constant
eff	Efficiency (*Ts* Total to Static, *Tt* Total to Total)
q(r)	Specific Blade Centrifugal Load Function
θ	Blade Lean Angle

References

1. Nichols, B. Design & Manufacture of Specialty Turbomachinery. Available online: https://www.barbernichols.com/sites/default/files/wysiwyg/images/turbine_selection_for_supercritical_co2_applications.pdf (accessed on 18 May 2018).
2. Boig, C.; Burkinshaw, M.; Todd, I. *The Application of Additive Manufacturing Toturbomachinery*; Institution of Mechanical Engineers: London, UK, 2018.
3. Almkvist, G.; Bjorkholtz, J.J.; Lindgren, E. PowerPulse. U.S. Patent US9,719,438 B2, 2017.
4. Hatton, G. Power Struggle. In *Racecar Engineering*; The Chelsea Magazine Company: London, UK, 2018; pp. 8–14.
5. Feneley, A.J.; Pesyridis, A.; Andwari, A.M. Variable Geometry Turbocharger Technologies for Exhaust Energy Recovery and Boosting-A Review. *Renew. Sustain. Energy Rev.* **2017**, *71*, 959–975. [CrossRef]
6. Karvountzis-Kontakiotis, A.; Alshammari, F.; Pesiridis, A.; Franchetti, B.; Pesmazoglou, I.; Tocci, L. Variable Geometry Turbine Design for Off-Highway Vehicle Organic Rankine Cycle Waste Heat Recovery. In Proceedings of the THIESEL 2016 Conference on Thermo-and Fluid Dynamic Processes in Direct Injection Engines, Valencia, Spain, 13–16 September 2016.
7. Persson, J. *1D Turbine Design Tool Validation and Loss Model Comparison: Performance Prediction of a 1-Stage Turbine at Different Pressure Ratios*; Kth Royal Institute of Technology: Stockholm, Sweden, 2015.
8. Ainley, D.G.; Mathieson, G.C.R. *An Examination of the Flow and Pressure Losses in Bfade Rows of Axial-Flow Turbines*; Ministry of Supply: London, UK, 1955.
9. Lozza, G. *A Comparison between the Craig-COX and the Kacker-Okapuu Methods of Turbine Performance Prediction*; Department of Energetics Politecnico di Milano: Milano, Italy, 1982.
10. Ennila, A.S.B. Prediction of Losses in Small Scale Axial Air Turbine Based. *Energy Procedia* **2015**, *75*, 3271–3276. [CrossRef]
11. Alshammari, F.; Karvountzis-Kontakiotis, A.; Pesyridis, A.; Usman, M. Expander Technologies for Automotive Engine Organic Rankine Cycle Applications. *Energies* **2018**, *11*, 1905. [CrossRef]
12. Ross, J.N. Ford Doubling 1.0L EcoBoost Engine Production. Available online: https://www.autoblog.com/2013/09/06/ford-doubling-1.0-liter-ecoboost-engine-production/?guccounter=1 (accessed on 1 August 2018).
13. Pesiridis, A.; Saccomanno, A.; Tuccillo, R.; Capobianco, A. Conceptual Design of a Variable Geometry, Axial Flow Turbocharger Turbine. In *SAE Technical Papers*; SAE International: Warrendale, PA, USA, 2017; Volume 2017-24-0163. [CrossRef]
14. Berchiolli, M.; Guarda, G.; Walsh, G.; Pesyridis, A. Turbocharger Axial Turbines for High Transient Response, Part 2: Genetic Algorithm Development for Axial Turbine Optimisation. *Appl. Sci.* **2019**, *9*, 2679. [CrossRef]
15. Herwig, H.; Schmandt, B. How to Determine Losses in a Flow Field: A Paradigm Shift towards the Second Law Analysis. *Entropy* **2014**, *16*, 2959–2989. [CrossRef]
16. Duhl, D.N.; Thompson, E.R. Directional Structures for Advanced Aircraft Turbine Blades. *J. Aircr.* **1977**, *14*, 521–526. [CrossRef]